




Magnetospheric Curvature Radiation by Bunches as Emission Mechanism for Repeating Fast Radio Bursts

Wei-Yang Wang (王维扬)^{1,2,3}, Yuan-Pei Yang (杨元培)⁴, Chen-Hui Niu (牛晨辉)³, Renxin Xu (徐仁新)^{1,2} , and Bing Zhang (张冰)⁵

¹ School of Physics and State Key Laboratory of Nuclear Physics and Technology, Peking University, Beijing 100871, People's Republic of China
wywang_astroph@pku.edu.cn

² Kavli Institute for Astronomy and Astrophysics, Peking University, Beijing 100871, People's Republic of China; r.x.xu@pku.edu.cn

³ National Astronomical Observatories, Chinese Academy of Sciences, Beijing 100101, People's Republic of China

⁴ South-Western Institute for Astronomy Research, Yunnan University, Kunming, Yunnan, 650500, People's Republic of China; pyyang@ynu.edu.cn

⁵ Department of Physics and Astronomy, University of Nevada, Las Vegas, NV 89154, USA

Received 2021 September 29; revised 2021 November 14; accepted 2021 December 6; published 2022 March 8

Abstract

Coherent curvature radiation as the radiation mechanism for fast radio bursts (FRBs) has been discussed since FRBs were discovered. We study the spectral and polarization properties of repeating FRBs within the framework of coherent curvature radiation by charged bunches in the magnetosphere of a highly magnetized neutron star. The spectra can be generally characterized by multisegmented broken power laws, and evolve as bunches move and the line of sight sweeps. Emitted waves are highly linear polarized and polarization angles are flat across the burst envelopes, if the line of sight is confined to the beam within an angle of $1/\gamma$, while a circular polarization fraction becomes strong for off-beam cases. The spectro-temporal pulse-to-pulse properties can be a natural consequence due to the magnetospheric geometry. We investigate the relationship between drift rate, central frequency, and temporal duration. The radius-to-frequency mapping is derived and simulated within the assumptions of both dipolar and quadrupolar magnetic configurations. The geometric results show that FRBs are emitted in field lines more curved than open field lines for a dipolar geometry. This suggests that there are most likely existing multipolar magnetic configurations in the emission region.

Unified Astronomy Thesaurus concepts: [Radio bursts \(1339\)](#); [Radio transient sources \(2008\)](#); [Radiative processes \(2055\)](#); [Neutron stars \(1108\)](#); [Magnetars \(992\)](#)

1. Introduction


The field of fast radio bursts (FRBs; Lorimer et al. 2007) enjoyed a rapid development from both the observational and theoretical frontiers (see Cordes & Chatterjee 2019; Petroff et al. 2019; Zhang 2020, for reviews). At present, hundreds of FRB sources have been discovered,⁶ and dozens of them can repeat (e.g., CHIME/FRB Collaboration et al. 2021). Although a large number of FRBs have been detected, the physical origin (s) of FRBs are still unknown. The discovery of a million Jansky FRB-like bursts from Galactic magnetar SGR J1935+2154 (Bochenek et al. 2020; CHIME/FRB Collaboration et al. 2020b) suggests that magnetars are the most likely candidate sources for at least some FRBs.

Regarding the nature of FRBs, observationally, the brightness temperature of FRBs can reach $\sim 10^{35}$ K, which demands an extremely coherent radiation mechanism. Melrose (2017) summarized three forms of coherence: radiation by bunches, reactive instabilities (or plasma masers), and kinetic instabilities (or vacuum masers). Most FRB models invoke neutron stars or magnetars to explain the milliseconds duration, high luminosity, and GHz emission frequency (e.g., see Platts et al. 2019, for a review). Based on the distance of the emission region from the neutron star, these models can be generally

divided into two categories (Zhang 2020): pulsar-like models (emission within the magnetosphere of a compact object; e.g., Kumar & Bošnjak 2020; Lu et al. 2020; Wang et al. 2020; Yang & Zhang 2021), and gamma-ray burst-like models (emission from relativistic shocks far outside the magnetospheres; e.g., Metzger et al. 2019; Beloborodov 2020; Margalit et al. 2020). There are some challenges from both the observational (Luo et al. 2020; Li et al. 2021; Nimmo et al. 2021) and theoretical (Lu & Kumar 2018; Lu et al. 2020) aspects for the latter models. In this paper, we mainly consider one type of pulsar-like model, which focuses on coherent curvature radiation by charged bunches to demonstrate its application to repeating FRBs.⁷

Polarization measurements are potential tools to reveal more original information about FRBs. Most FRBs usually have strong linear polarization, which is generally dozens of a percent, with some even close to 100% (e.g., Michilli et al. 2018; Day et al. 2020; Luo et al. 2020), but some also have significant circular polarization fractions (Hilmarsson et al. 2021b; Kumar et al. 2021; Xu et al. 2021). These properties are similar to those of pulsars, which show a wide variety of polarization fractions between sources but with noticeable differences. At least a fraction of pulsars whose S-shaped polarization angle (PA) swing can be characterized by the rotation vector model (Lorimer & Kramer 2012). However, while some FRBs (FRB 121102, FRB 180916) exhibit a flat PA across each pulse (Michilli et al. 2018; Nimmo et al. 2021),

⁶ See Transient Name Server, <https://www.wis-tns.org/>.

 Original content from this work may be used under the terms of the [Creative Commons Attribution 4.0 licence](https://creativecommons.org/licenses/by/4.0/). Any further distribution of this work must maintain attribution to the author(s) and the title of the work, journal citation and DOI.

⁷ It is an open question whether all FRBs repeat. Observationally, FRBs fall into two groups: repeaters and apparently nonrepeating FRBs. We mainly focus on repeaters in this paper.

some others (e.g., FRB 180301, FRB 181112) show variable PAs across each burst (Cho et al. 2020; Luo et al. 2020), and FRB 20201124A shows both flat and evolving PAs (Hilmarsson et al. 2021b; Kumar et al. 2021).

FRBs have been reported in detection from 110 MHz to at least 8 GHz (Gajjar et al. 2018; Pastor-Marazuela et al. 2021). The spectral indices are volatile, ranging from -10 to $+14$ if they are modeled by simple power laws (Spitler et al. 2016). This may imply a narrow-band spectrum with an intrinsic hardening spectral index at low frequencies. Within the framework of coherent curvature radiation by bunches, Yang et al. (2020) proposed that charge separation between the electron and positron clumps can explain the narrow-band spectrum.

Notably, a very intriguing spectral pattern has been found in at least some repeaters. These repeaters exhibit a clear time–frequency downward drifting, that is, the central frequency of consecutive sub-bursts with later-arriving time have lower frequencies (CHIME/FRB Collaboration et al. 2019a, 2019b; Hessels et al. 2019; Josephy et al. 2019; CHIME/FRB Collaboration et al. 2020a; Fonseca et al. 2020; Day et al. 2020; Li et al. 2021; Platts et al. 2021). The downward drifting structure is nicknamed the “sad trombone” effect. However, rarely does there also exist a possible upward-drifting event (the “happy trombone” effect) for some bursts (Chawla et al. 2020; CHIME/Frb Collaboration et al. 2020a; Hilmarsson et al. 2021a; Kumar et al. 2021). The two peaks of the FRB-like event from SGR J1935+2154 seem to be consistent with such a pattern (Bochenek et al. 2020; CHIME/FRB Collaboration et al. 2020b).

There have been several models proposed to explain these spectro-temporal characteristics. Within the framework of magnetospheric curvature radiation, we proposed a generic geometric model to explain the downward drifting pattern (Wang et al. 2019). Invoking a possible time difference in launching the sparks, we show that a small fraction of FRBs can show an upward-drifting pattern (Wang et al. 2020). Other mechanisms intrinsic to the FRB sources include magnetar-wind-driven external shock (Metzger et al. 2019), asteroid falling (Liu et al. 2020), blast waves from flares (Beloborodov 2020), a relativistic moving source (Rajabi et al. 2020), and free–free absorption (Kundu & Zhang 2021), which have been proposed to interpret the downward drifting features. Models invoking propagation effects, e.g., plasma lensing (Cordes et al. 2017) or scintillation (Simard & Ravi 2020) can account for both upward and downward drifting patterns but are challenged by the fact that the majority of drifting patterns are downdrift.

In this paper, we attempt to interpret the spectral and polarization properties of FRBs within the framework of coherent curvature radiation by bunches in the magnetosphere of a magnetar. The pulse-to-pulse properties are explained by the geometric model and we confront the model with the repeater data. The paper is organized as follows. We discuss the dynamics of moving charges and their radiation properties in Section 2. The pulse-to-pulse properties are demonstrated and applied to derive radius-to-frequency mapping in Section 3. The results are discussed and summarized in Section 4. The convention $Q_x = Q/10^x$ in cgs units is used throughout the paper.

2. Burst from Moving Charges in the Magnetosphere

In contrast to the continuous “sparking” processes in the polar cap region of normal pulsars that produce particle bunches (Ruderman & Sutherland 1975), FRB emissions are believed to be triggered by a sudden and violent mechanism. Here we do not discuss the trigger mechanism but attempt to study the radiation properties from the bunched particles that likely formed during the violent triggering process. For a relativistic charged particle in a strong magnetic field, the vertical momentum perpendicular to the field line drops to zero rapidly, so that its trajectory essentially tracks with the magnetic field lines. When these charged particles stream outward along the magnetic field lines and enter the charge starvation region, they are accelerated by the electric field parallel to the B field. A photon-pair production cascade may be triggered, which mimics the sparking processes in the inner magnetosphere of radio pulsars but with a much larger amplitude.

Basically, electron-positron pairs are created by such a sparking mechanism, move along the curved trajectories, and emit curvature radiation due to the perpendicular acceleration. Curvature radiation from charged bunches has been invoked to interpret both coherent radio emission of pulsars (e.g., Ruderman & Sutherland 1975; Sturrock et al. 1975; Elsaesser & Kirk 1976; Cheng & Ruderman 1977; Melikidze et al. 2000; Gil et al. 2004; Gangadhara et al. 2021) and FRBs (e.g., Katz 2014; Kumar et al. 2017; Ghisellini & Locatelli 2018; Katz 2018; Lu & Kumar 2018; Yang & Zhang 2018; Wang & Lai 2020; Wang et al. 2020; Cooper & Wijers 2021a).

As the bunches flow out along the field lines, they corotate with the neutron star. The observed duration of an FRB due to the possible rotation is

$$w \sim \frac{\min(\theta_{\text{jet}} P/2\pi, t_{\text{int}})}{1+z}, \quad (1)$$

where θ_{jet} is the burst “jet” beaming angle, P is the period, z is the redshift, and t_{int} is the intrinsic duration of the FRB (Yang et al. 2019).

2.1. Charged Particles in the Magnetosphere

A neutron star may undergo a sudden trigger (e.g., crust cracking), which sustains at least milliseconds. Such a process likely creates many sudden and violent sparking events. These sparking events may generate bunches via two-stream instabilities (Usov 1987; Asseo & Melikidze 1998; Melikidze et al. 2000). Bunches are numerically simulated to form in open field lines through a cascading process (Philippov et al. 2020). Benáček et al. (2021) found an overlap of the fastest particles with consecutively emitted bunches in the momentum space via particle-in-cell simulations. This overlap drives two-stream instabilities, causing up to $\sim 15\%$ of the initial kinetic energy transformed into electric field energy and eventually to radiation.

When the size of the charged bunch is smaller than the half-wavelength, waves are coherently enhanced significantly. However, the charges moving in different trajectories (different distances to the triggering source) produce different photon arrival delays, which leads to the incoherence of radiation. Charges in the bunch that are projected in the horizontal plane would have the same phase. As shown in Figure 1, for instance, the charges⁸ within a light red slice (a bunch) are created at the same time and travel the same distance, emitting

⁸ Positive net charges are the point of interest in the following discussion.

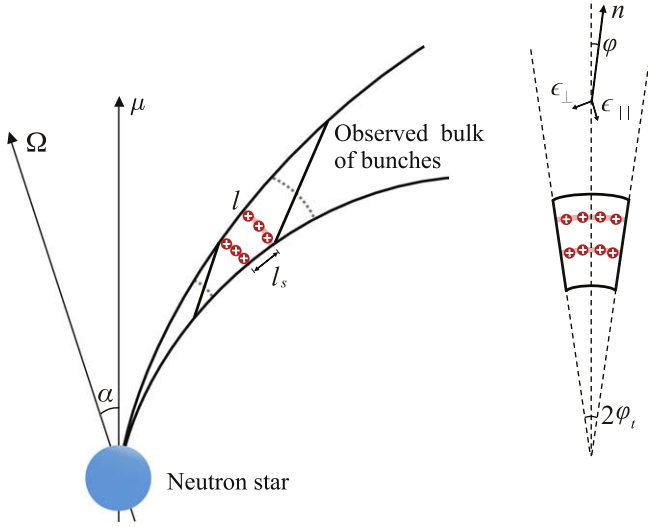


Figure 1. Schematic diagram of a bulk of bunches contributing to instantaneous radiation. In the left panel, within the moving bulk, the light solid red line shows the slice in which charges emit roughly the same phase. Therefore, two red lines present two bunches. The bunch length is l with the mean space between each bunch l_s in the laboratory frame. The gray dotted lines denote average heights for both upper and lower boundaries of the bulk. The bulk seen in the horizon plane is shown in the right panel. The unit vector of the line of sight is denoted by \mathbf{n} , and ϵ_{\parallel} and ϵ_{\perp} denote the two polarization components (see Appendix B). The opening angle of the bulk of the emission region is $2\varphi_i$.

electromagnetic waves that are added coherently. The emission from a charge is coherently added within one bunch but incoherently bunch to bunch if $l_s > \lambda/2$.

Emitting bunched particles are most likely produced in the open field lines rather than closed field lines, where there may be absorption caused by bunches moving along adjacent field lines (e.g., Yang & Zhang 2018). The magnetic field is much stronger near the polar cap region, leading to possibly more dramatic activities. Multipolar magnetic fields may exist near the stellar surface and may be dominant by at least several tens of stellar radii. It makes field lines more curved and equivalently enlarges the polar cap angle of the open field lines. In the following calculations, the spherical coordinates (r, θ, φ) with respect to the magnetic axis are used.

Consider generally geometric expressions of the magnetic field configuration. We discuss the simplest case where the field lines are axisymmetric (see Appendix A). Combined with the Maxwell equations and the force-free condition, a magnetic field configuration solution is given by Equations (A5), (A7). The parameter n denotes the order of the multipoles, e.g., $n = 1$ for dipole, $n = 2$ for quadrupole, etc. Regardless of the value of n , some self-similar features for multipolar configuration can be summarized as follows:

1. The trajectory family with the same polar angle θ has the same tangent direction;
2. Curvature radius is only proportional to r for the trajectory family with the same polar angle θ , see Equation (A9);
3. θ_{\max} is smaller for a high- n multipolar configuration due to more curved field lines;
4. The magnetic field strength is generally in the form of $B \simeq B_s(R/r)^{2n+1}$, where B_s is the field strength at the stellar surface and R is the stellar radius;

5. For any $\theta \ll 1$, the distance that charges traveled along the field lines is $s \approx r$.

A generic expression for the volume of bunches in the lab frame is given by (see Appendix A)

$$V_b \simeq \lambda \varphi_i r^2 \frac{f'(\theta_s)}{f'(\theta)} \Delta\theta_s, \quad (2)$$

where θ_s is the angle of the footpoint for each field line at the stellar surface. The term of $f'(\theta_s)/f'(\theta)$ depends on n . For small θ values, the magnetic field lines are not curved enough, so that $f'(\theta_s)/f'(\theta)$ is roughly of the order of unity.

For an antiparallel rotator, the polar cap region is populated with net positive charges. Positrons produce radiation as the outflow streams along the curved B -field lines. However, the typical cooling timescale is much shorter than the FRB duration, so that there must be an electric field E_{\parallel} parallel to the B field to sustain the energy of charged particles (Kumar et al. 2017). The E_{\parallel} enables pairs to decouple and the radiation would not cancel out (Yang et al. 2020). Generally, the acceleration of a charged bunch can be described as

$$N_e E_{\parallel} e ds - \mathcal{L}_b dt = N_e m_e c^2 d\gamma, \quad (3)$$

where N_e is the number of net charges in one bunch that are radiating coherently, c is the speed of light, e is the elementary charge, m_e is the positron mass, γ is the Lorentz factor of the bunch, and \mathcal{L}_b is the luminosity of a bunch.

Charges in the bunch are suggested to move along nearly identical orbits, therefore they act like a single macro charge, which emits a power N_e^2 times p_e , where p_e is the curvature radiation luminosity for one positron, which reads $2e^2\gamma^4 c/(3\rho^2)$, where ρ is the curvature radius. As shown in Figure 1, there could be N_b bunches contributing to instantaneous radiation in the bulk, but the emissions from them are added incoherently, leading to an incoherent summation of the curvature radiation power, i.e., $\mathcal{L} = N_b N_e^2 p_e$, where N_b is the number of independent bunches that contribute to the observed luminosity at an epoch. The number N_b can be estimated as $\sim 10^5 r \gamma \gamma_2^{-1} \theta_{-1}^{-1}$ (emission within a conal angle of $1/\gamma$ can be seen at $\omega = \omega_c$, see Section 2.3).

The observed isotropic luminosity should be compared with the isotropic equivalent luminosity from the model, which is given by (Kumar et al. 2017)

$$\mathcal{L}_{\text{iso}} \approx \gamma^4 N_b N_e^2 p_e \approx 4.6 \times 10^{42} \gamma_2^8 N_b 5 N_{e,22}^2 \rho_7^{-2} \text{ erg s}^{-1}, \quad (4)$$

Consequently, the radiation power is always balanced with the electric power provided by the E_{\parallel}

$$E_{\parallel} v_e \simeq N_e p_e, \quad (5)$$

where v_e is the velocity of the positron. Regardless of the initial energy distribution of the charges, they will eventually be modulated by the E_{\parallel} in the magnetosphere. According to Equation (5), the required E_{\parallel} to sustain the radiation power is given by

$$E_{\parallel} \simeq \frac{2\gamma^4 N_e e}{3\rho^2} \simeq 3.2 \times 10^6 \gamma_2^4 N_{e,22} \rho_7^{-2} \text{ esu}. \quad (6)$$

The timescale for the radiation power that can be balanced by E_{\parallel} is essentially the cooling timescale of the bunches, which

can be estimated as

$$t_c \approx \frac{N_e \gamma m_e c^2}{\mathcal{L}_b} \approx 1.8 \times 10^{-12} \rho_7^2 \gamma_2^{-3} N_{e,22}^{-1} \text{ s}. \quad (7)$$

This timescale is much shorter than the FRB duration. This suggests that particles essentially stay balanced throughout the FRB emission process.

At lower heights, the volume of a bunch can be calculated as

$$V_b \approx 3.0 \times 10^{10} \varphi_{t,-2} \nu_9^{-1} r_7^2 \Delta \theta_{s,-3} \text{ cm}^3. \quad (8)$$

In the lab frame, the number density of net charge can be estimated as

$$n_e = \frac{N_e}{V_b} \approx 3.3 \times 10^{11} N_{e,22} \varphi_{t,-2}^{-1} \nu_9 r_7^{-2} \Delta \theta_{s,-3}^{-1} \text{ cm}^{-3}. \quad (9)$$

Therefore, the required multiplicity is

$$\mathcal{M} = \frac{n_e}{n_{\text{GJ}}} \approx 4.8 \times 10^{2n-2} N_{e,22} P_0 \varphi_{t,-2}^{-1} \nu_9 B_{s,15}^{-1} r_7^{2n-1} \Delta \theta_{s,-3}^{-1}, \quad (10)$$

where the Goldreich–Julian density is (Goldreich & Julian 1969)

$$n_{\text{GJ}} = \frac{|\boldsymbol{\Omega} \cdot \mathbf{B}|}{2\pi c e}, \quad (11)$$

and Ω is the angle frequency of a neutron star. The slow rotation can let $\mathcal{M} > 1$ (Cooper & Wijers 2021b).

2.2. Breakout of FRB Waves

An important requirement for FRBs to be observed is the successful escape of radio waves from the magnetosphere. Near the emission region, even the electric field of the electromagnetic wave E is very large, the electron motion is confined to be along magnetic field lines. The oscillation of charged particles would not be relativistic in the presence of the electromagnetic wave. Compared to the vacuum case, the speed of them is suppressed by a factor of $(\omega/\omega_B)^2$, where ω_B is the cyclotron frequency:

$$\omega_B = \frac{eB}{m_e c} \approx 1.8 \times 10^{21-2n} B_{s,15} r_7^{-2n-1} \text{ rad s}^{-1}. \quad (12)$$

A strength parameter can be defined as $a = eE/m_e c \omega$. The electric amplitude can be calculated as $E \approx 8.2 \times 10^8 \mathcal{L}_{42}^{1/2} r_7$ esu, leading to $a = 2.3 \times 10^6 \mathcal{L}_{42}^{1/2} r_7 \nu_9^{-1}$. As the wave propagates away from the magnetosphere in a decreasing background field $B \propto r^{-2n-1}$, E would exceed the background field at r_0 :

$$r_0 = \left(B_s R^{2n+1} \sqrt{\frac{c}{2\mathcal{L}}} \right)^{1/2n} \approx (1.2 \times 10^5 B_{s,15})^{1/2n} R. \quad (13)$$

For instance, $r_0 \approx 3.5 \times 10^2 R$ for a dipole and $r_0 \approx 18.7R$ for a quadrupole.

When the FRB propagates in the magnetosphere, the nonlinear effect due to the relativistic oscillation of electrons under the coherent electromagnetic wave is involved (Yang & Zhang 2020). For X-mode photons⁹ with E much smaller than

⁹ The two polarization states of electromagnetic radiation in the presence of a strong magnetic field can be described as those in which the electric vector is perpendicular to the magnetic and wavevector plane (X mode) and those with electric vector in that plane (O mode).

the background magnetic field B , the electron cross section is

$$\sigma \simeq \begin{cases} (\omega/\omega_B)^2 \sigma_T, & \omega \ll \omega_B \\ \sigma_T, & \omega \gg \omega_B \end{cases}. \quad (14)$$

Beyond the region $r \gtrsim 10^8$ cm in a dipolar field, the wave amplitude is stronger than the background magnetic strength, leading to the possibility that the magnetosphere is optically thick to FRBs, i.e., $\tau_{sc} \simeq n_e r a^2 \sigma \gg 1$, due to the enhanced scattering (Beloborodov 2021).

However, even if the magnetosphere is opaque to the FRB, the FRB can break out from the magnetosphere medium once its radiation pressure exceeds the plasma pressure in the magnetosphere, $P_{\text{rad}} \gg P_{\text{gas}}$. The radiation pressure caused by the bunches is

$$P_{\text{rad}} = \frac{\mathcal{L}}{4\pi r^2 c} \approx 2.7 \times 10^{16} \mathcal{L}_{42} r_7^{-2} \text{ dyn cm}^{-2}. \quad (15)$$

The pressure of the pair gas can be estimated as $P_{\text{gas}} \simeq n_{\text{gas}} k_B T_{\text{gas}}$, where n_{gas} is the number density of gas, k_B is the Boltzmann constant and T_{gas} is the temperature of gas. Considering that surrounding gas should not be denser and hotter than bunches, i.e., $n_{\text{gas}} < n_e$ and $k_B T_{\text{gas}} < \gamma m_e c^2$, one can obtain

$$P_{\text{gas}} < n_e \gamma m_e c^2 \approx 2.7 \times 10^7 N_{e,22} \gamma_2 \varphi_{t,-2}^{-1} \nu_9 r_7^{-2} \Delta \theta_{s,-3}^{-1} \text{ dyn cm}^{-2}. \quad (16)$$

Therefore, the radiation pressure of the FRB can readily push aside and break out of the surrounding pair medium, so that both O- and X-mode radio waves may be observable (e.g., Ioka 2020).

2.3. Spectrum

Consider the radiation from the bulk of bunches in the magnetosphere. The observed emission cannot be simply demonstrated by the summation of the curvature radiation power of individual particles, since FRB emissions must be coherent. The bunch length in the radial direction is $\sim 10\nu_9^{-1}$ cm, much smaller than the curvature radius of the trajectory. This allows a point-source approximation. The E_{\parallel} -induced acceleration is balanced by the radiation of charged particles, sustaining a constant velocity $v_e \simeq c$, and constant- γ positron distribution.

The energy per unit time per unit solid angle is

$$\frac{d^2 W}{dt d\Omega} = \frac{c}{4\pi} |\mathbf{E}(t) \mathcal{R}|^2, \quad (17)$$

where \mathcal{R} is the distance from the emitting source to the observer. The spectral information can be obtained from Fourier transformation, leading to

$$\frac{d^2 W}{d\Omega d\omega} = c |\mathbf{E}(\omega) \mathcal{R}|^2. \quad (18)$$

Contained in $\mathbf{E}(\omega)$ is all the information about the frequency behavior of $\mathbf{E}(t)$. Note that this is the total energy per solid angle per frequency range in the entire pulse, and there is no ‘‘per unit time’’ in its dimension, due to the violation of the uncertainty relation $\Delta\omega \Delta t > 1$ (Rybicki & Lightman 1979).

If the pulses repeat on an average timescale T , one can obtain

$$\frac{d^2W}{d\omega d\Omega dt} \equiv \frac{1}{T} \frac{d^2W}{d\omega d\Omega}. \quad (19)$$

However, the definition of radiation power for curvature radiation from a single charge is no longer meaningful, because the charge motion direction only sweeps the line of sight (LOS) once. For coherent radiation from more than one bunch sweeping across the LOS, T here would be the mean time interval of each coherent pulse, and $d^2W/d\Omega d\omega$ corresponds to the radiation energy of one coherent pulse (Yang & Zhang 2018).

According to Equation (6), the Lorenz factor of charges strongly depends on the location in the magnetosphere due to the rapid balance between E_{\parallel} and radiation. A delta function distribution of the positron Lorenz factor in a macro-charged bunch is adopted, which is different from the simple power-law distribution hypothesized by Yang & Zhang (2018). In this section, we assume that bunches are uniformly distributed in all directions of $(\hat{r}, \hat{\theta}, \hat{\varphi})$ in three-dimensional bunches. Any particle could be described by three subscripts (i, j, k) , which contain all the information of the location. If there is more than one charged particle, one can replace the single amplitude with the sum of the amplitudes. The total energy radiated per unit solid angle per unit frequency interval for the moving charges in the magnetosphere can be written as

$$\frac{d^2W}{d\omega d\Omega} = \frac{e^2\omega^2}{4\pi^2c} \times \left| \int_{-\infty}^{+\infty} \sum_i N_s \sum_j N_{\theta} \sum_k N_{\varphi} - \beta_{e\perp,ijk} e^{i\omega[t - n\cdot r_{ijk}(t)/c]} dt \right|^2, \quad (20)$$

where $N_s, N_{\theta}, N_{\varphi}$ are the maximum numbers for i, j, k , and the total number of positrons is $N = N_s N_{\theta} N_{\varphi}$ (see Appendix B).

Charged particles move along different trajectories with different phases and orientations. The frequency-dependent spread angle is found as (Jackson 1998)

$$\theta_c(\omega) \simeq \begin{cases} \frac{1}{\gamma} \left(\frac{2\omega_c}{\omega} \right)^{1/3} = \left(\frac{3c}{\omega\rho} \right)^{1/3}, & \omega \ll \omega_c \\ \frac{1}{\gamma} \left(\frac{2\omega_c}{3\omega} \right)^{1/2}, & \omega \gg \omega_c \end{cases}, \quad (21)$$

where ω_c is the critical frequency of curvature radiation, which reads $\omega_c = 3c\gamma^3/(2\rho)$. For $\omega \sim \omega_c$, the conal beam angle is $\sim 1/\gamma$. The observed length of the emitting region can be estimated as $\sim \rho\gamma^{-1}\theta^{-1} \sim 1.0 \times 10^6 \rho\gamma_2^{-1}\theta_{-1}^{-1}$ cm, which is much smaller than $c\omega \sim 3 \times 10^7$ cm. As a result, there should be persistent bunches traveling through the emitting region during the FRB emission.

In order to obtain the spectrum of electromagnetic waves, the polarized amplitudes of the waves could be described by deriving two orthogonal components, i.e., A_{\parallel} and A_{\perp} (see Appendix B), which contain the information not only of amplitude but also of phase. For a single charge, A_{\parallel} is earlier than A_{\perp} by $\pi/2$ in phase.

We calculate the amplitude of electromagnetic waves for any particle with a given trajectory (see Appendix B for details). The coherent condition of the trajectories with different curvature radii is satisfied, due to $\Delta\rho \sim \rho/\gamma \ll 2^{5/3}\pi\rho/3$ for $\omega \approx \omega_c$ (Yang & Zhang 2018). Therefore, the total energy

radiated per unit solid angle per unit frequency interval for the moving bunches is given by

$$\frac{d^2W}{d\omega d\Omega} = N_{lb} \frac{e^2\omega^2}{4\pi^2c} \left| \sum_i^{N_l} \sum_j^{N_{\theta}} \sum_k^{N_{\varphi}} - \epsilon_{\parallel} A_{\parallel,ijk} + \epsilon_{\perp} A_{\perp,ijk} \right|^2, \quad (22)$$

where N_l is the number of positrons inside each bunch and N_{lb} is the number of bunches.

We define a characteristic frequency

$$\omega_l = \frac{2c}{l}. \quad (23)$$

Since the mean space between charged particles increases as the bunches move away from the magnetosphere, bunch size continuously increases with increasing height. If $\omega \ll \omega_l$, one would have the half wavelength $l < \lambda/2$, so that charges in the bunch emit roughly the same phase. Otherwise, the term $\sin^2(\omega/\omega_l)/(\omega/\omega_l)^2$ will play a role in reducing coherence (see Appendix B).

Charges in different trajectories may have different azimuth angles. We define

$$\omega_{\varphi} = \frac{3c}{\rho(\chi'^2 + \varphi'^2)^{3/2}}. \quad (24)$$

Here, χ' and φ' can let ω_{φ} reach the minimum value of ω_{φ} , which is defined as ω_r . Note that we only investigate the cases for either $1/\gamma < \varphi'$ or $1/\gamma < \chi'$, since the total flux for both $1/\gamma < \varphi'$ and $1/\gamma < \chi'$ is extremely small. For instance, if $\omega \ll \omega_r$ ¹⁰ the LOS is confined to the beam within $1/\gamma$. One may define $\varphi < 1/\gamma$ as on-beam and $\varphi > 1/\gamma$ for off-beam. For the on-beam case, the summation of A_{\perp} is extremely small due to axial symmetry matching the calculations from Yang & Zhang (2018). We develop the Yang & Zhang (2018) model by invoking the off-beam cases and calculating the spectra and polarization properties.

There are several regimes for the spectrum:

- (a) $\omega_c \ll \omega_r, \omega_c \ll \omega_l$: The spectrum is shown in Figure 2 panel (a), and its formula can be referred to Equation (B15). The spectrum could be regarded as that of a single charge multiplied by a factor of $N_e^2 N_b$. The peak energy radiated per unit solid angle per unit frequency interval is given by
$$\frac{d^2W}{d\omega d\Omega} \Big|_{\max} \simeq N_b N_e^2 \left(\frac{\chi_u - \chi_d}{\Delta\theta_s} \right)^2 \frac{3e^2\gamma^2}{2^{2/3}\pi^2c} \Gamma(2/3)^2. \quad (25)$$
- (b) $\omega_l \ll \omega_l \ll \omega_c$: For $\omega_l < \omega_c$, not all of the radiation energy in the bunch opening angle can be observed. For $\omega \ll \omega_l$, the spectral formula can be referred to Equation (B20). If $\omega \gg \omega_l$, the formula should be multiplied by a factor of $(\omega_l/\omega)^2$. The spectrum is shown in panel (b) of Figure 2. If $\chi' \gg \varphi'$, the peak energy radiated per unit solid angle

¹⁰ Assuming $\chi' \ll \varphi'$ here. For $\varphi' \ll \chi'$, one can replace φ' by χ' .

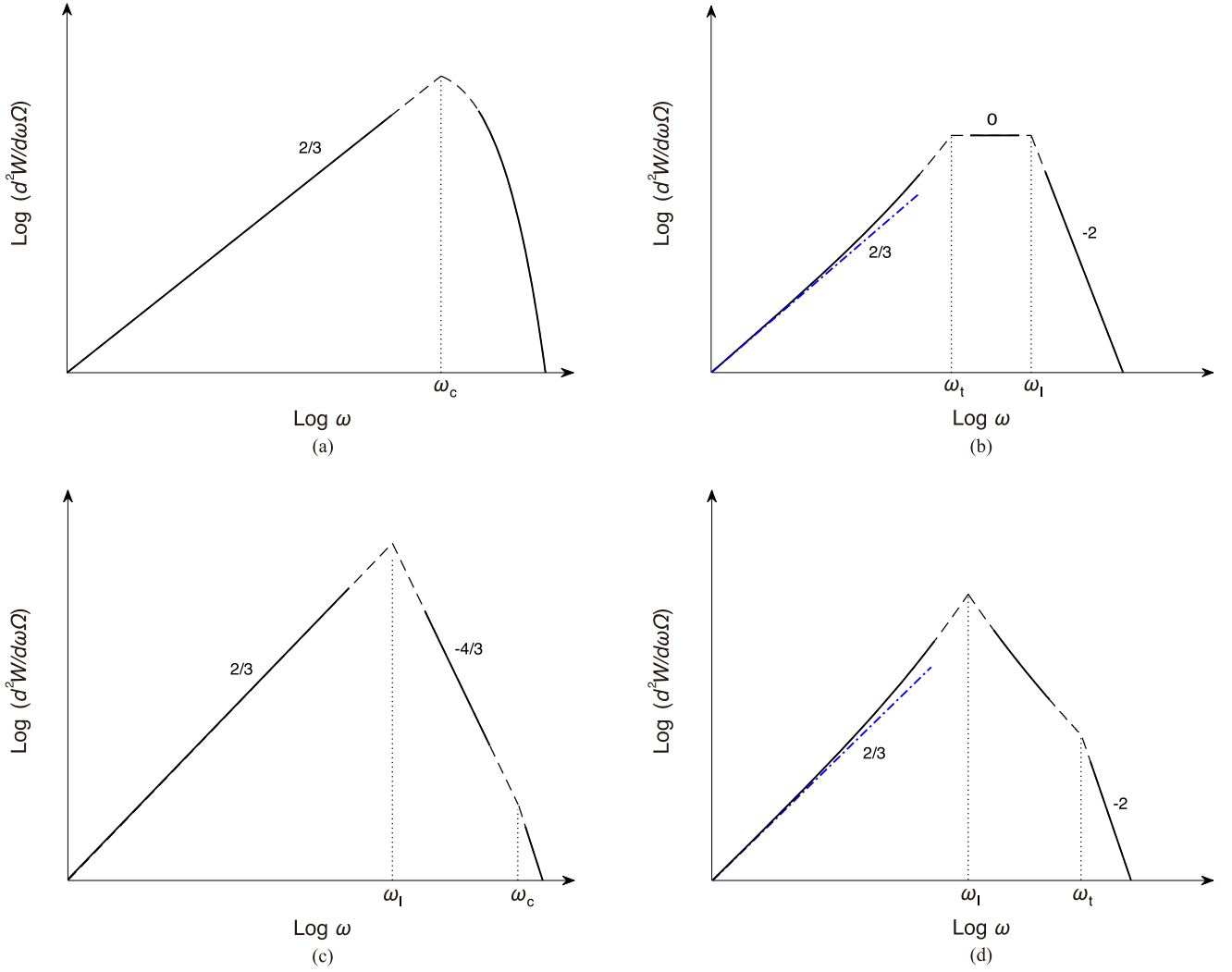


Figure 2. The spectra of the coherent curvature radiation: (a) $\omega_c \ll \omega_l$ and $\omega_c \ll \omega_j$; (b) $\omega_l \ll \omega_j \ll \omega_c$; (c) $\omega_l \ll \omega_c \ll \omega_j$; (d) $\omega_l \ll \omega_j \ll \omega_c$. The blue dashed-dotted lines denote power-law spectra with an index of $2/3$.

per unit frequency interval is given by

$$\frac{d^2W}{d\omega d\Omega} \Big|_{\max} \simeq N_b N_e^2 \left(\frac{\chi_u - \chi_d}{\Delta\theta_s} \right)^2 \frac{3e^2\gamma^2}{4\pi^2 c} \left(\frac{2\omega_l}{\omega_c} \right)^{2/3} \times \left[\Gamma(2/3)^2 + \frac{\gamma^2}{4^{2/3}} \left(\frac{\chi_u + \chi_d}{2} \right)^2 \Gamma(1/3)^2 \left(\frac{\omega_l}{\omega_c} \right)^{2/3} \right]. \quad (26)$$

On the other hand, if $\chi' \ll \varphi'_{\text{ase}}$, it is

$$\frac{d^2W}{d\omega d\Omega} \Big|_{\max} \simeq N_b N_e^2 \left(\frac{\chi_u - \chi_d}{\Delta\theta_s} \right)^2 \frac{3e^2\gamma^2}{4\pi^2 c} \left(\frac{2\omega_l}{\omega_c} \right)^{2/3} \times \left[\Gamma(2/3)^2 + \frac{\gamma^2}{4^{2/3}} \varphi'^2 \Gamma(1/3)^2 \left(\frac{\omega_l}{\omega_c} \right)^{2/3} \right]. \quad (27)$$

- (c) $\omega_l \ll \omega_c \ll \omega_j$: This case is the same as in case (a) but there should be multiplied by a factor of $(\omega_l/\omega)^2$ for $\omega_l \ll \omega$. The spectrum is shown in panel (c) of Figure 2.
- (d) $\omega_l \ll \omega_j \ll \omega_c$: The bunch length-induced incoherence appears at $\omega < \omega_j$. The spectrum is shown in panel (d) of Figure 2. The peak energy radiated per unit solid angle per unit frequency interval is similar to case (b), but one should replace ω_l with ω_j .

The spectrum can evolve as the bunches flow out from the magnetosphere. The mean space $l_s \propto r$, making high-frequency waves become incoherent at higher altitudes, e.g., spectra become harder, as shown in Figure 2, evolve from (a) to (c), or (b) to (d). The LOS is initially off-beam, then approaches the axis within $1/\gamma$ to become on-beam, and finally becomes off-beam again as the LOS sweeps across the emission region. Consequently, the spectrum evolves from (b) to (a) and then back to (b), or (d) to (c) and then back to (d).

2.4. Polarization

We consider the polarization of emission from the moving charged bunches. Basically, for a single particle, if $\varphi_k = 0$, the LOS would sweep in the trajectory plane, and only A_{\parallel} can be seen. Consequently, the radiation is 100% linearly polarized. Circular polarization would be seen and become stronger for off-beam observations. However, the deviation of the LOS from the direction of the velocity makes the observed flux decrease rapidly.

For more than one emitting particle, the polarization could be derived from the summation of the electric field vector of the waves. The Fourier transformed components of $\mathbf{E}(\omega)$ in the

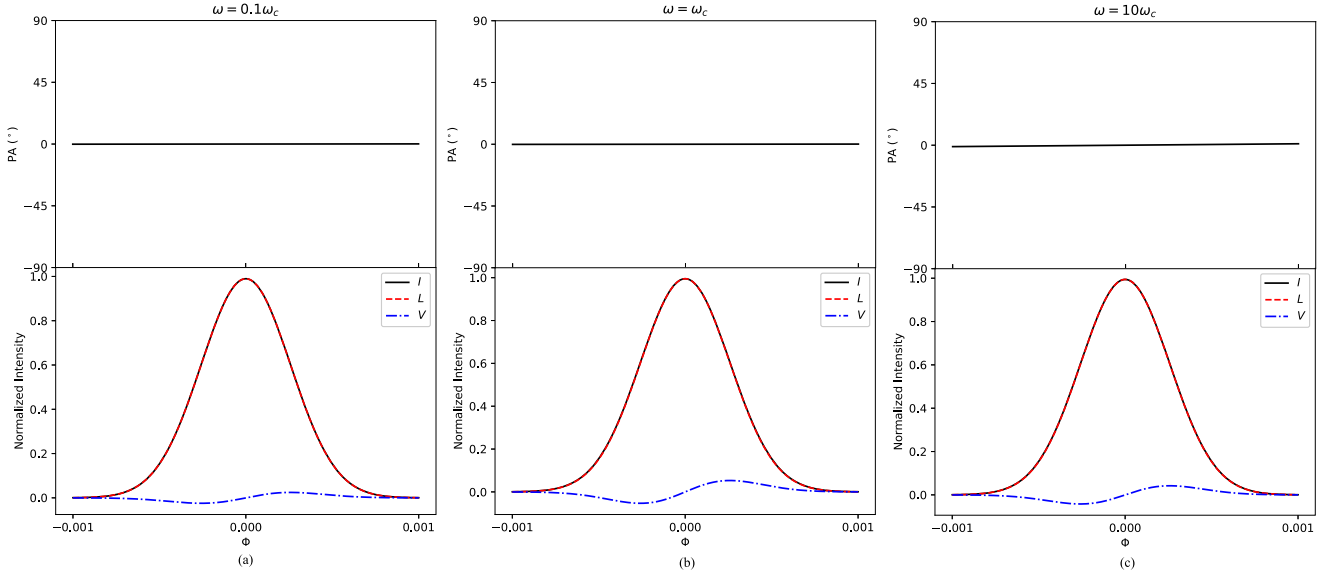


Figure 3. Simulated polarization profile and PA across the burst envelope for different frequencies: (a) $\omega = 0.1\omega_c$; (b) $\omega = \omega_c$; (c) $\omega = 10\omega_c$. Polarized intensities are plotted in colored solid lines. Parameters are adopted as $\alpha = \pi/6$, $\zeta = \pi/4$, $\gamma = 100$, $\varphi_t = 0.001$, $\Phi_p = 0$ and $\sigma_w = \varphi_t/2$.

directions ϵ_{\parallel} and ϵ_{\perp} are given by

$$E_{\parallel}(\omega) = \frac{e\omega A_{\parallel}}{2\pi cR}, \quad E_{\perp}(\omega) = \frac{e\omega A_{\perp}}{2\pi cR}. \quad (28)$$

If the LOS sweeps the axis of symmetry of the emission region, i.e., $\Phi = 0$, the summation of A_{\perp} appears to cancel out each other, leading to 100% linear polarization. For off-beam observations, $\sum A_{\perp} \neq 0$, so that the linearly polarized component decreases while the circularly polarized component becomes stronger.

The Stokes parameters can be calculated as

$$\begin{aligned} I &= \mu(A_{\parallel}A_{\parallel}^* + A_{\perp}A_{\perp}^*), \\ Q &= \mu(A_{\parallel}A_{\perp}^* - A_{\perp}A_{\parallel}^*), \\ U &= \mu(A_{\parallel}A_{\perp}^* + A_{\perp}A_{\parallel}^*), \\ V &= -i\mu(A_{\parallel}A_{\perp}^* - A_{\perp}A_{\parallel}^*), \end{aligned} \quad (29)$$

where $\mu = \omega^2 e^2 / (4\pi^2 \mathcal{R}^2 cT)$ is the proportionality factor. Here, the chosen way is such that I is the flux density repeated on the average timescale T . The corresponding PA is then given by

$$\Psi = \frac{1}{2} \tan^{-1} \left(\frac{U}{Q} \right), \quad (30)$$

where

$$\begin{pmatrix} U_s \\ Q_s \end{pmatrix} = \begin{pmatrix} \cos 2\psi & \sin 2\psi \\ -\sin 2\psi & \cos 2\psi \end{pmatrix} \begin{pmatrix} U \\ Q \end{pmatrix}, \quad (31)$$

in which ψ is given by the rotation vector model (Radhakrishnan & Cooke 1969) as a function of azimuthal angle with respect to the spin axis Φ :

$$\tan \psi = \frac{\sin \alpha \sin \Phi}{\cos \alpha \sin \zeta - \cos \zeta \sin \alpha \cos \Phi}. \quad (32)$$

When the LOS sweeps across the emission region as the neutron star spins, and if particles happen to be moving into the

bulk region, pulsed emissions can be seen. Here we assume that the plasma density in the emission region is Gaussian-modulated in the azimuthal direction. The electric field vector should be multiplied by a modulation function

$$f(\phi) = f_0 \exp \left[- \left(\frac{\Phi - \Phi_p}{\sigma_w} \right)^2 \right], \quad (33)$$

where Φ_p is the peak location of the Gaussian function, i.e., at the center of emission region, f_0 is the amplitude and σ_w is the Gaussian width.

Consider a quadrupole magnetic configuration. We assume that $\Delta\theta_s = 0.002$ and $r = 10^7$ cm. Adopting $f_0 = 1$, $\sigma_w = \varphi_t/2$ and $\Phi_p = 0$, we simulate the polarization profile and PA across the burst envelope in three frequency cases ($\omega = 0.1\omega_c$, $\omega = \omega_c$, $\omega = 10\omega_c$), under the assumption of $\varphi_t = 10^{-3}$, $\gamma = 100$, $\alpha = \pi/6$ and $\zeta = \pi/4$ as shown in Figure 3. We then consider the polarization properties related to different geometric conditions. The polarization properties are simulated with different decl. angles, Gaussian widths, and peak locations in panel (b) of Figure 4.

The radiation is highly polarized, i.e., $I^2 = L^2 + V^2$, as in the case of 100% elliptically polarized radiation, where $L^2 = Q^2 + U^2$ denotes a linearly polarized component. According to the calculation in Section 2.3, if $\varphi' \ll 1/\gamma$ and $\chi' \ll 1/\gamma$, the circular polarization fraction can be estimated as $|V|/I \sim 2|A_{\perp}/A_{\parallel}|$. It would reach the maximum value at $\omega \sim \omega_c$. In Figure 3, $|L|/I > 94\%$ and $|V|/I < 33\%$ within the pulse window, lead to a highly linear polarization fraction. The ratio $|L|/I > 98\%$ and $|V|/I < 18\%$ within the pulse window in panel (a) and (c) of Figure 4, and $|L|/I > 94\%$ and $|V|/I < 30\%$ for panel (b) of Figure 4.

All figures show a flat PA across the burst envelope. The PA evolves within 2° as shown in Figure 3. For different geometric conditions, PA also evolves at most within 6° (see Figure 4). Different geometrical conditions can change the width of pulse window, but slightly affect the circular polarization fraction.

The circular polarization fraction becomes stronger as φ_t gets larger. We consider the cases that $\varphi_t = 0.007$. Particles

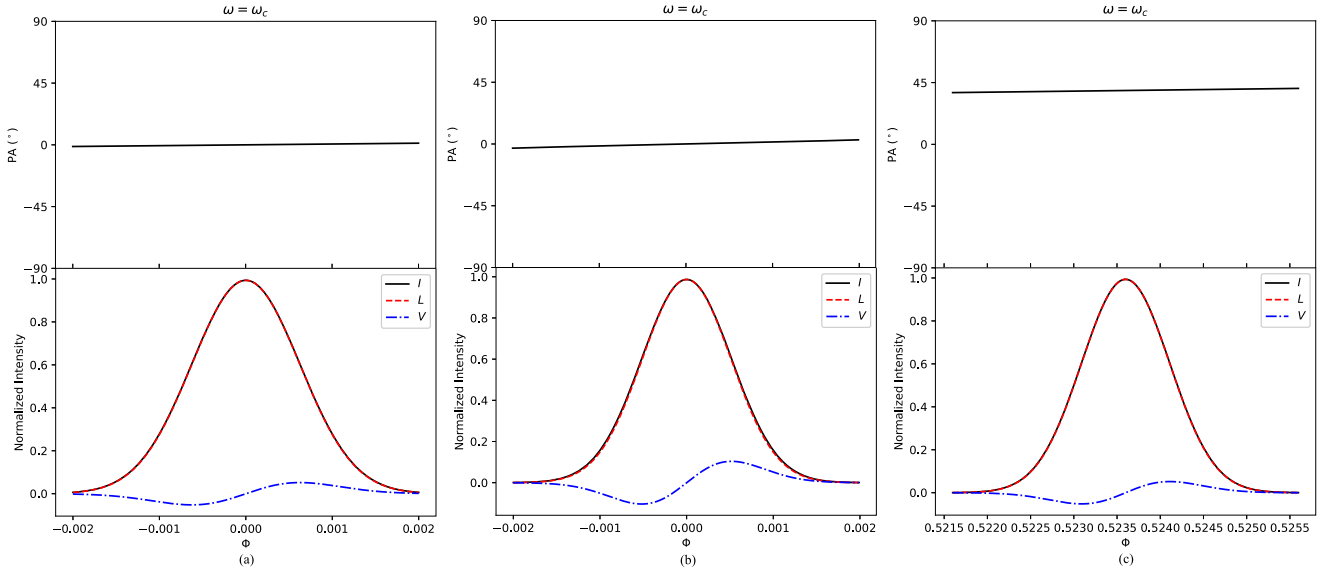


Figure 4. The same as panel (b) in Figure 3 but for different parameters: (a) $\alpha = \pi/18$, $\zeta = \pi/3$, $\sigma_w = \varphi_i/2$, $\Phi_p = 0$; (b) $\alpha = \pi/6$, $\zeta = \pi/4$, $\sigma_w = \varphi_i$, $\Phi_p = 0$; (c) $\alpha = \pi/6$, $\zeta = \pi/4$, $\sigma_w = \varphi_i/2$, $\Phi_p = \pi/6$.

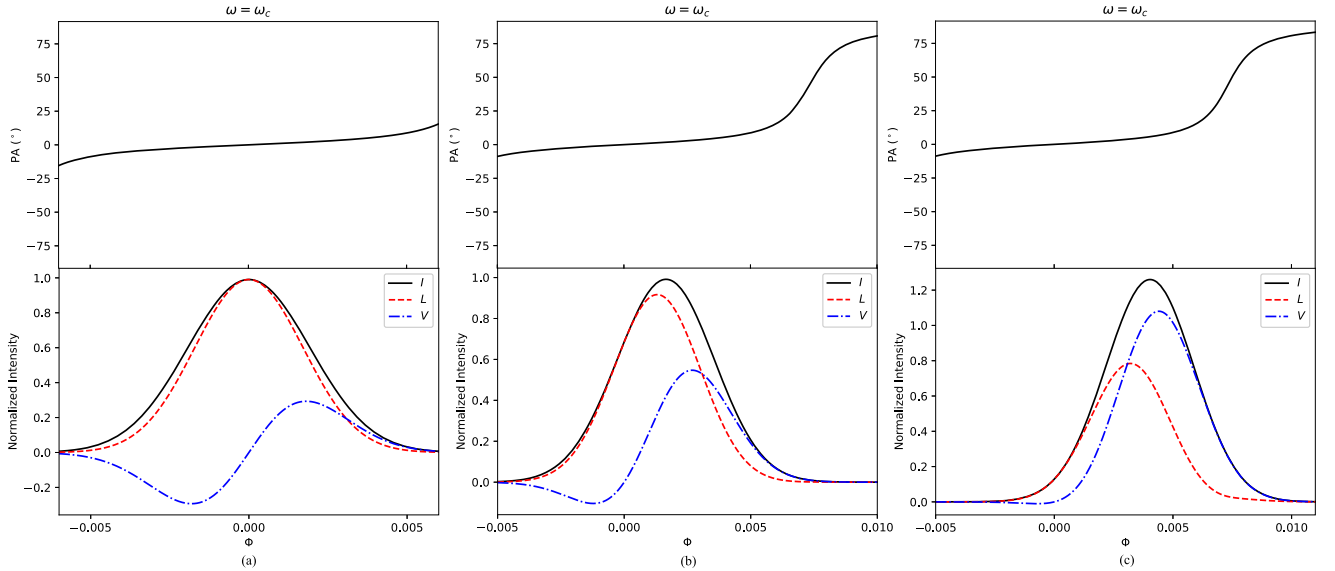


Figure 5. The same as panel (b) in Figure 3 but for $\varphi_i = 0.7\gamma^{-1}$ with different parameters: (a) $\Phi_p = 0$; (b) $\Phi_p = 0.002$; (c) $\Phi_p = 0.005$.

distributed in bunches can affect the summation of amplitudes, hence, are considered with different forms. The polarization profile and PA across the burst envelope with different charge distributions for $\varphi_i = 0.7\gamma^{-1}$ are simulated and illustrated in Figure 5. Within the pulse window, all three panels in Figure 5 exhibit $|V/I| > 50\%$. Circular polarization can dramatically grow when the peak location of the particle distribution deviates from the geometric center. PAs evolve as S-shapes in panels (b) and (c), which is generally consistent with some observations of highly circular polarized bursts (Kumar et al. 2021; Xu et al. 2021).

For the off-beam case, A_{\perp} would be comparable with A_{\parallel} when $\omega \sim \omega_r$, leading to a highly circular polarization fraction. We simulate the polarization profile and PA across the burst envelope at $\omega = \omega_c$ for $\varphi_i = 0.1$ in Figure 6. The parameters are adopted as follows: $\alpha = \pi/6$, $\zeta = \pi/4$ and $\Phi_p = 0$ for panel (a); $\alpha = \pi/18$, $\zeta = \pi/6$ and $\Phi_p = 0$ for panel (b); $\alpha = \pi/6$, $\zeta = \pi/4$ and $\Phi_p = \pi/6$ for panel (c). For all the simulated cases, waves are highly linearly polarized but a $\sim 100\%$ circular polarization

exists at near $|\varphi| \simeq \varphi_i$. However, the flux for the off-beam case is extremely lower than that of the on-beam case. The PA evolves within 20° for panel (a) and 14° for panels (b) and (c). The PA across the burst envelope more dramatically changes with the magnetospheric geometry compared with the case of $\varphi' \ll 1/\gamma$.

3. Pulse-to-pulse Properties

3.1. Drift Pattern of Subpulse

As the magnetosphere rotates, magnetic field lines sweep across the LOS and there may be more than one bulk of bunches being observed coincidentally. As shown in Figure 7, line 1 and line 2 are approximately in the same plane due to slow rotation. However, FRB sources can repeat so that it is hard to distinguish whether the observed two pulses are the subpulses of one burst or indeed two individual pulses. The “subpulse” emission discussed here, is intrinsically identified as

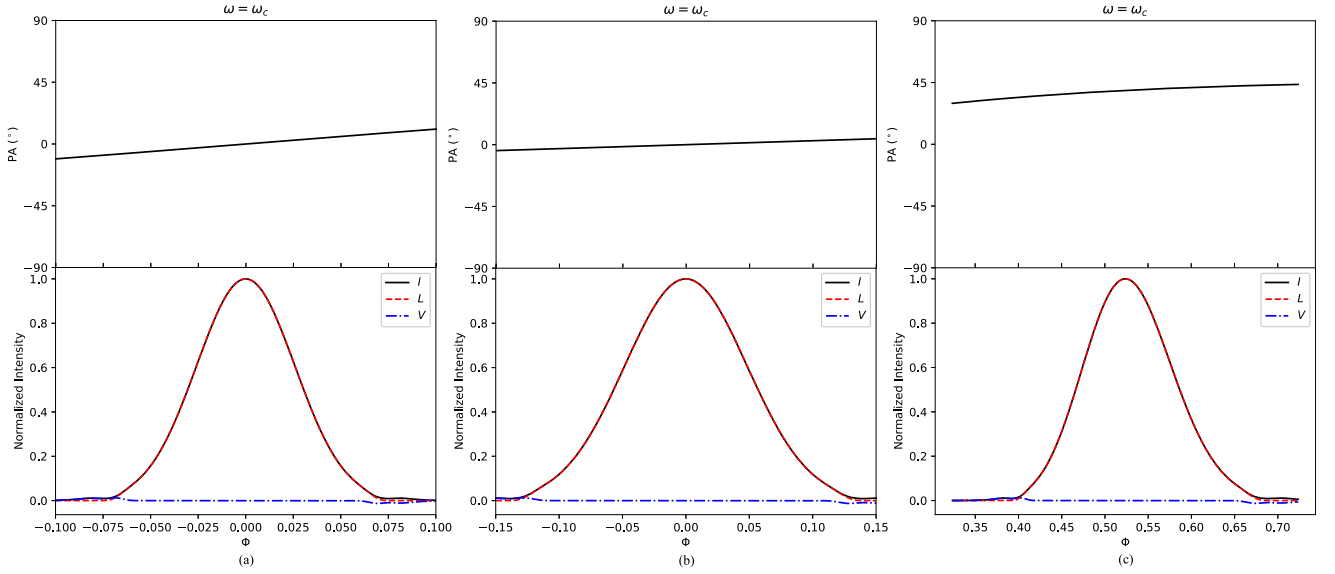


Figure 6. The same as panel (b) in Figure 3 but for $\varphi_i = 10\gamma^{-1}$ with different parameters: (a) $\alpha = \pi/6$, $\zeta = \pi/4$ and $\Phi_p = 0$; (b) $\alpha = \pi/18$, $\zeta = \pi/6$ and $\Phi_p = 0$; (c) $\alpha = \pi/6$, $\zeta = \pi/4$ and $\Phi_p = \pi/6$.

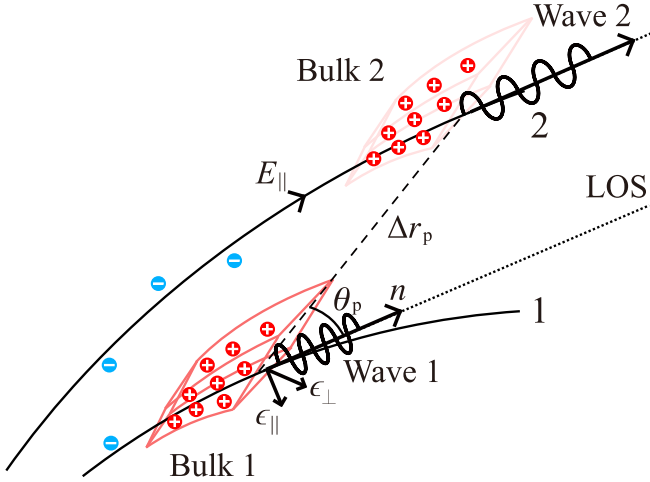


Figure 7. A schematic diagram of moving charges in the magnetosphere. For instance, the observer could see emissions from the two bulks of neighboring magnetic field lines 1 and 2. The dotted lines show the LOS. The two emitting points for wave 1 and wave 2 are different in radius and in azimuthal angle.

bursts emitted by sparking events from the same trigger event on the stellar surface. The trigger event may last a long time, but subpulses are observed within one period.

The temporal and frequency properties of subpulses are supposed to be strongly related to the magnetospheric geometry. The time delay for the two waves reads

$$\Delta t = t_{20} - t_{10} + \Delta t_{\text{geo}}, \quad (34)$$

where t_{10} and t_{20} are the times when the bunches are generated, and Δt_{geo} is the geometric time delay, which can be calculated as

$$\Delta t_{\text{geo}} = \frac{s_2 - s_1}{v_{e,\parallel}} - \frac{\Delta r_p \cos \theta_p}{c}, \quad (35)$$

where Δr_p denotes the distance between the points where emission can sweep the LOS at two magnetic field lines, i.e., two emitting points, and $v_{e,\parallel}$ is the velocity of the positrons parallel to the B -field lines (Wang et al. 2020). From

Equation (A7) and (A8), the distance $\Delta r_p = \Delta r$ if the neutron star rotates very slowly, i.e., $\Delta t_{\text{obs}} \ll P$. The velocity $v_{e,\parallel} \simeq \beta_e c$ when charges are far from the light cylinder. Footpoints of the field lines are located in the polar region so that we have $\theta_0 \ll 1$ and then Equation (35) can be written as

$$\Delta t_{\text{geo}} \simeq \frac{\Delta r}{c} \left[\left(1 + \frac{1}{2\gamma^2} \right) I_n(\theta) - \cos \theta_p \right], \quad (36)$$

where $I_n(\theta)$ is a dimensionless parameter denoting the enhancement factor due to the field line curvature (see Appendix A).

First, we consider that charges are triggered at the same time, i.e., $t_{20} = t_{10}$. Combining Equations (5), (36) and the specific geometric condition of the magnetic field, one can obtain

$$\dot{\nu} = \left[\frac{1}{2} \frac{\Delta \rho}{\rho \Delta t} + \frac{3}{4} \left(\frac{\partial E_{\parallel}}{E_{\parallel}} \frac{\Delta r}{\Delta t} + \frac{\partial E_{\parallel}}{E_{\parallel}} \frac{\partial t}{\partial t} \right) \right] \nu. \quad (37)$$

In the following discussion, we assume that E_{\parallel} is independent of time, i.e., $\partial E_{\parallel} / \partial t = 0$. From Equation (5), in order to derive a constant Lorentz factor, one requires that $E_{\parallel} \propto r^{-2}$. Then, the drift pattern can be described as $\dot{\nu} \propto -\nu^2$. More complicated time–frequency structures could originate from E_{\parallel} with more complex formulae.

A bunch roughly has a thickness of half a wavelength, contributing to the FRB radiation for a time duration of the order of ν^{-1} in the observer frame. The thickness becomes larger as the bunch moves to a higher altitude. According to Equation (1), if the neutron star rotates slowly, a continuous plasma flow emits for a duration of $w \propto N_B \nu^{-1}$, where N_B is the total number of bunches generated during the trigger. The pulse width is related to ν , e.g., $w \propto \nu^{-1}$, which leads to $\dot{\nu} \propto -\nu/w$.

We investigate the relationship between drift rate and burst central frequency. All parameters are considered in the rest frame of the host galaxy. Therefore, one has $\nu = \nu_{\text{obs}}(1+z)$, $\dot{\nu} = \dot{\nu}_{\text{obs}}(1+z)^2$, and $w = w_{\text{obs}}/(1+z)$. The observed width is derived from autocorrelation functions by fitting a two-dimensional Gaussian (Chamma et al. 2021). Most repeaters

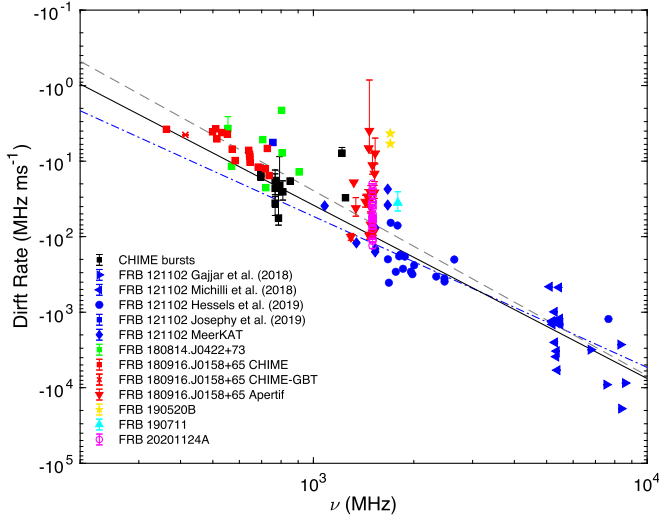


Figure 8. Drift rates at different frequencies. Both drift rates and frequencies are transferred in the rest frame of the host galaxy. Different repeaters are presented in different colors: FRB 121102 (blue), FRB 180814.J0422+73 (green), FRB 180916.J0158+65 (red), FRB 190711 (cyan), FRB 20201124A (purple), FRB 190520B (yellow), and other CHIME bursts (black). The gray dashed line shows the best fit through the data for all FRBs. The black solid dashed line is the best fit for FRB 121102 with a power-law index of 2.29 and the blue dashed-dotted line for that with a frozen index of 2.00.

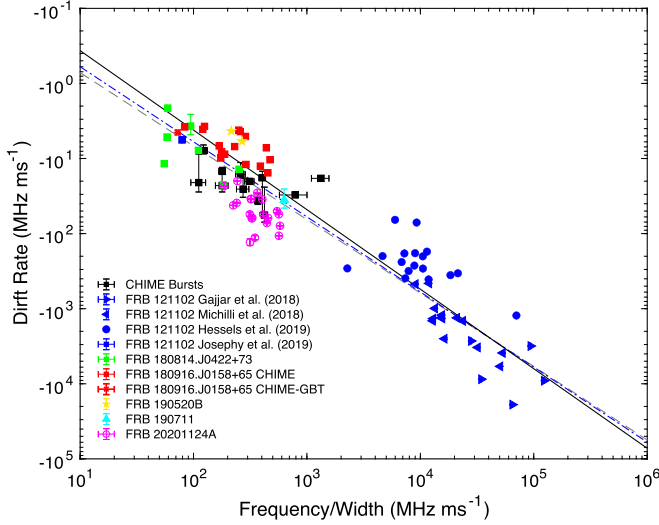


Figure 9. Same as Figure 8 but for drift rates at different ratios of frequency to subpulse width.

have measured redshifts. For the sources without precise redshift measurements, their redshifts are calculated from the dispersion measure (DM) models (see, e.g., Deng & Zhang 2014; Zhang 2018; Pol et al. 2019; Cordes et al. 2021).

The relationship between $\dot{\nu}$ and the central frequency as well as $\dot{\nu}$ and the ratio of ν/w are plotted in Figures 8 and 9. These relationships have been used to fit the data for several repeaters (Chamma et al. 2021). Here, we expand our sample and apply these observed results in the rest frame of their host galaxies. The data are quoted from Gajjar et al. (2018), Michilli et al. (2018), CHIME/FRB Collaboration et al. (2019a), CHIME/FRB Collaboration et al. (2019b), Hessels et al. (2019), Josephy et al. (2019), Caleb et al. (2020), Chamma et al. (2021), Chawla et al. (2020), Day et al. (2020), Pastor-Marazuela et al. (2021), Hilmarsson et al. (2021b),

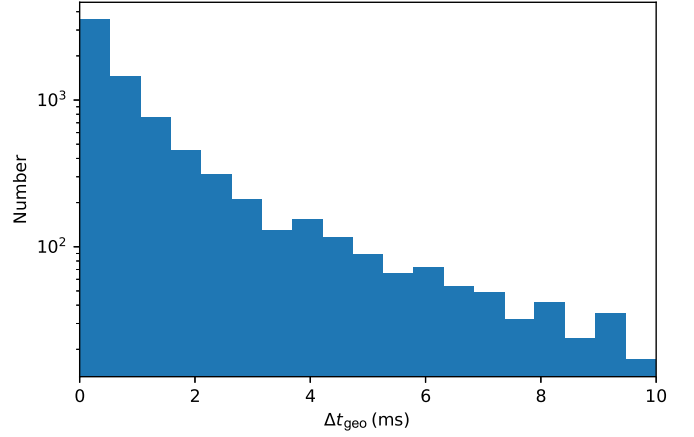


Figure 10. Histograms of estimated Δt_{obs} for quadrupole from Equation (38).

and Platts et al. (2021). Note that the observed central frequencies for the CHIME bursts (black squares in Figures 8 and 9) are adopted as 600 MHz and 1370 MHz for FRB 20201124A (Hilmarsson et al. 2021b). The details of data analysis for FRB 190520B are shown in Appendix C.

We fit both the $\dot{\nu} - \nu$ and $\dot{\nu} - \nu/w$ relationships. The fitting is first considered for FRB 121102, which exhibits the most multiband data. Both the $\dot{\nu} - \nu$ and $\dot{\nu} - \nu/w$ relationships can be well fitted by power laws: $\dot{\nu} = -5.0_{-4.7}^{+83.1} \times 10^{-6} \nu^{2.29 \pm 0.36}$ and $\dot{\nu} = -3.2_{-3.0}^{+57.0} \times 10^{-2} (\nu/w)^{1.06 \pm 0.31}$. We then fix the power-law index as 2 and 1 for $\dot{\nu} - \nu$ and $\dot{\nu} - \nu/w$ fitting, and the results are given by $\dot{\nu} = -5.4_{-1.1}^{+1.4} \times 10^{-5} \nu^2$ and $\dot{\nu} = -5.5_{-1.7}^{+2.5} \times 10^{-2} \nu/w$. Finally, we fit both relationships to power laws for all FRBs. The results are the following: $\dot{\nu} = -1.1_{-0.8}^{+3.4} \times 10^{-6} \nu^{2.45 \pm 0.21}$ and $\dot{\nu} = -7.6_{-3.7}^{+7.3} \times 10^{-2} (\nu/w)^{0.97 \pm 0.09}$.

3.2. Subpulse Interval

There are rare FRBs exhibiting upward-drifting structures. Regardless of whether two or more pulses are subpulses of a single burst or truly multiple bursts, the observed interval is generally described by Equation (34). Consequently, if the trigger event has a long duration, there would be a higher chance to observe upward-drifting events (Wang et al. 2020). For a short-duration triggering mechanism ($|t_{20} - t_{10}| \ll \Delta t_{\text{geo}}$), the observed interval for two subpulses is determined by

$$\Delta t_{\text{geo}} = I_n(\theta) \frac{R}{nc} \left[\frac{f(\theta)}{f(\theta_s)} \right]^{1/n} \Delta \ln[f(\theta_s)]. \quad (38)$$

Based on Equation (38), we plot the simulated distribution of the observed time intervals for a quadrupole field with 10^4 samples, as shown in Figure 10. We fix θ at θ_{max} for the quadrupole. The events where $\Delta t_{\text{geo}} < 0.1$ ms are ignored. Two angles θ_{s1} and θ_{s2} are uniformly distributed in the range of $0 - 0.06^{11}$ rad in the simulations. The simulated interval is generally consistent with the sub-burst separation distribution from Pleunis et al. (2021).

¹¹ The maximum $\theta_s = 0.06$ is adopted, which is θ_{max} at the location of $r = 10R$.

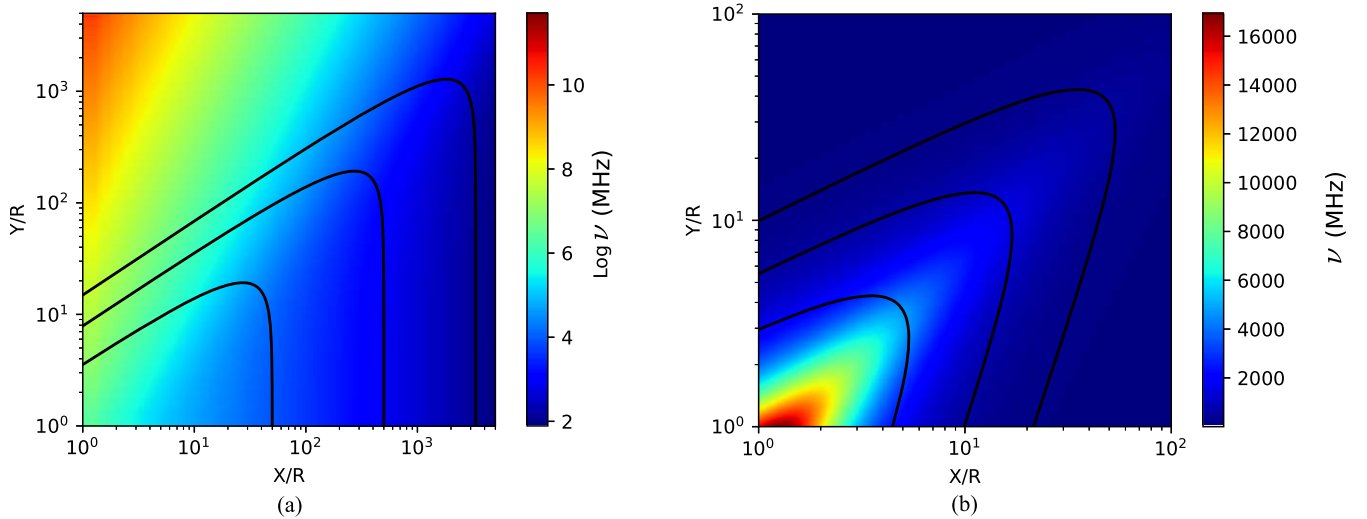


Figure 11. Radius-to-frequency mapping derived by the drifting pattern for two cases: (a) dipole; (b) quadrupole. Black solid lines denote magnetic field lines.

3.3. Radius-to-frequency Mapping

The drifting pattern of FRBs reflects the radiation frequency change with the location in the magnetosphere, i.e., the so-called “radius-to-frequency mapping” (e.g., Wang et al. 2019). For all sparking particles created at the same time, if γ is a constant, combining Equations (35), (37) and specific geometry conditions as discussed in Section 2.1, one can derive

$$\dot{\nu} = -\frac{4\pi C_n(\theta)}{3\gamma^3 [I_n(\theta) - \cos \theta_p]} \nu^2, \quad (39)$$

where $C_n(\theta)$ is a geometric factor (see Equation (A10)).

We first consider a dipolar configuration. Combining the fitting results of FRB 121102 with Equation (39), we plot the radius-to-frequency mapping of the magnetosphere, shown in panel (a) of Figure 11. The observed FRB frequency ranges from 110 MHz to $\gtrsim 8$ GHz. The pulse-to-pulse temporal property is caused by the geometric effect, i.e., different emitting bunches (sparks) traveling in different trajectories exhibit different photon arrival delays. However, aberrations of light can reduce the trajectory-induced interval. From Equation (35), we can obtain $\Delta r \simeq c\Delta t_{\text{geo}} \sin^2 \theta$ for $\theta \sim 0.1$. In order to create millisecond burst intervals, the distance between two emission regions should be $\Delta r \sim 10^3 R$.

Another possible scenario is that radio waves are produced at closed field lines. The aberration term could be neglected for a dipolar configuration when $\theta \sim \pi/2$, so that we have $\Delta r_{\text{geo}} \simeq c\Delta t_{\text{obs}}/I_1(\pi/2)$. The emission region is located at $r \gtrsim 10R$.

We then consider a quadrupolar configuration. Based on Equation (39), the spectro-temporal properties strongly depend on the polar angle of LOS. However, the trajectory plane that truly sweeps across the LOS is random. If $\theta > \theta_{\text{max}}$, particles would move toward the stellar surface, resulting in the radiation beam not being swept by the LOS. For $\theta \ll 0.5$, the quadrupole has similar geometric properties as the dipole. Beyond that region, quadrupolar field lines are more curved, so that the particles should travel a longer distance than the dipole case to reach the emitting points. For $\pi/5 \lesssim \theta$, the aberration term is not an order of magnitude larger than the interval traveled. The interval distance is $\Delta r \simeq c\Delta t_{\text{obs}}/I_2(\theta_{\text{max}})$. In order to generally match the fitting results, we adopt $\gamma = 100$ and plot

the radius-to-frequency mapping, shown in panel (b) of Figure 11. FRBs are suggested to be emitted at several to hundreds of stellar radii.

4. Conclusion and Discussion

In this paper, we developed a general radiation theory of coherent curvature radiation of charged bunches in the magnetosphere from the first principle and applied the model to interpret the spectral and polarized emission properties of repeating FRBs. Within this framework, we considered the spectro-temporal pattern by deriving a generic magnetic configuration and modeled the observed drift rates for some FRBs. The following conclusions can be drawn:

- (1) We consider a general scenario that charged bunches move in a rotating magnetosphere with a multipolar magnetic field. The emitting bunches have a specific configuration as defined by the magnetic field lines. Trajectories (field lines) for charges are not parallel to each other, which allows the angle of LOS with respect to the central axis to enter the problem. Combining with the considered magnetic field configuration, we calculated the predicted radiation spectra, which can be generally characterized by multisegmented broken power laws, and evolve with the motion of bunches and rotation of the neutron star. The total flux for an on-beam case is higher than that of an off-beam case.
- (2) For a uniformly distributed particle in bunches, the emission is 100% linearly polarized when the LOS is parallel to the central axis. The sign of circular polarization will change when the LOS is parallel to the symmetric axis of the bulk. If the opening angle of the bulk is smaller than $1/\gamma$ ($\omega_c < \omega_l$), that is, an on-beam case, the emission keeps being highly linearly polarized as the LOS sweeps across the emitting bunches, with a flat PA across the burst envelope. The circular polarization fraction becomes stronger as $|\varphi|$ grows due to the nonaxisymmetric summation of A_{\perp} . High circular polarization events are rarely observed, suggesting that most bunches have small opening angles in those cases. PA across the burst envelope is more dramatic than that of the on-beam case. A luminous and highly circular

polarized pulse may be generated when $\varphi_r \sim 1/\gamma$ or when particles are extremely nonuniformly distributed in bunches. Both linear and circular polarization fractions are frequency dependent and the waves are 100% polarized.

- (3) The radiation front pushes aside the pair plasma and can break out of the magnetosphere, forming a charge starvation region. In this region, an electric field might be produced and quickly balanced with the electric power provided by E_{\parallel} . The required E_{\parallel} is smaller than that proposed by Kumar et al. (2017), where only the kinetic energy was considered.
- (4) We expand the geometric model (Wang et al. 2019, 2020), where only the dipolar field was considered, to a more general scenario by invoking multipolar fields. Within the framework of curvature radiation, the spectro-temporal property of subpulses can be naturally modeled by the geometric model. Such a drifting structure would appear at some single pulses from a pulsar with an FRB-like trigger mechanism. For a constant γ , regardless of the magnetic configuration, the observed drift rate generally follows $\dot{\nu} \propto -\nu^2$. The drift rate as a function of frequency for FRB 121102 can be well fitted by the model and a generic power law with index 2.29 ± 0.36 . For the sample of all FRBs, the best power-law fitting result is 2.45 ± 0.19 . The drift rate as a function of ν/w can be also fitted by a power law. The indices are 1.06 ± 0.31 for FRB 121102 and 0.97 ± 0.09 for all FRBs.
- (5) Based on the geometric model, the spectro-temporal properties suggest that the radiation site varies in the magnetosphere. We derive the radius-to-frequency mapping within both dipolar and quadrupolar scenarios. For the dipolar scenario, the observed FRBs are suggested to be emitted at $r \gtrsim 10R$ in closed field lines. This results from satisfying geometric conditions. A quadrupolar configuration has more curved field lines, so that emission height is at several to hundreds of stellar radii, lower than that of the dipolar scenario. FRB sources are most likely to host multipolar fields or more curved magnetic configurations than an ideal dipole.

According to the rotation vector model (Radhakrishnan & Cooke 1969), the PA is generally flat for a slow-rotating pulsar, but evolves at the smallest impact angle. Within this scenario, the flatness of PA across the burst envelope and extremely highly linear polarization fraction of the emission of FRB 121102, FRB 180916, and FRB 20201124A suggest that neutron stars rotate slowly ($P > 1$ s) with a small opening angle. Flat PA across the burst envelope but with $\sim 10\%$ circular polarization when $\varphi_r = 0.1\gamma^{-1}$ matches the observation of FRB 20201124A. If the multipolar components have the same axis as the dipole, the PA across the burst envelope can also be characterized by the S-shape rotation vector model. Variable PA across the burst envelope (FRB 180301, FRB 181112) may require more complicated magnetic field configurations and LOS geometry, or propagation effects operating either inside the magnetosphere or far from the source (e.g., Dai et al. 2021).

A triple subpulse burst has been found in FRB 121102 (burst 6, MJD 58075; see Hilmarsson et al. 2021a). An apparent upward-drifting pattern can be seen between the first two components, while the second and third components exhibit a downward drifting pattern. The PA of the first component differs from those of the other two. Based on the geometric

model, as the magnetosphere sweeps across the LOS, one would first observe an upward-drifting pattern, and after the LOS crosses the minimum impact angle, a downward drifting pattern. During this process, PA evolves as an S-shape according to the classical rotation vector model.

According to Equation (37), the fluctuation of the drift rate may be related to the fluctuation of the particle number and the inclination of the LOS. Most repeating FRBs have the same order of drift rate at the same central frequency, suggesting that these sources most likely have similar magnetospheres. Surprisingly, such drift pattern has also been discovered in at least some single pulses of PSR B0950+08, but with lower frequency bands (20–83 MHz) (Bilous et al. 2022). Rajabi et al. (2020) proposed a dynamical model in which the drift rate is a function of ν/w because of the relativistic motion. However, within the curvature radiation model, the burst duration depends on the number of bunches that travel through as the LOS sweeps the radiation region, e.g., $w \sim N_B \nu^{-1}$. Consequently, the relationship $\dot{\nu} \propto \nu/w$ gives rise to $\dot{\nu} \propto \nu^2$.

This paper focuses on coherent curvature radiation by bunches. Recently, Zhang (2022) proposed another general class of models invoking coherent inverse Compton scattering by bunches. The spectra and polarization properties of that model require detailed investigations.

The authors are grateful to Mohammed Chamma and Henning Hilmarsson for providing data. We are also grateful to Xuelei Chen, Shi Dai, Clancy James, Jinchun Jiang, Jiguang Lu, Rui Luo, Donald Melrose, Lijing Shao, Jumpei Takata, Hao Tong, Zhen Yan, Jumei Yao, Haoyang Ye, Bin-Bin Zhang, Song-Bo Zhang, and an anonymous referee for helpful comments and discussions. This work is supported by the National Key R&D Program of China No. 2017YFA0402602 and the National SKA Program of China No. 2020SKA0120100. W.-Y.W. is supported by a Boya Fellowship and the fellowship of China Postdoctoral Science Foundation No. 2021M700247. Y.-P.Y. is supported by NSFC grant No. 12003028. C.-H.N. is supported by a FAST Fellowship. R.X. is supported by the Strategic Priority Research Program of CAS (XDB23010200).

Appendix A Magnetosphere Geometry

In this section, we briefly summarize the geometric properties of magnetic configuration. Generally, with the assumption of axisymmetric force-free condition, the flux function obeys the Grad–Shafranov equation

$$\frac{\partial^2 A}{\partial r^2} + \frac{1-x^2}{r^2} \frac{\partial^2 A}{\partial x^2} + F(A) \frac{dF}{dA} = 0, \quad (\text{A1})$$

where $x = \cos \theta$ and $F(A)$ is the free function. The magnetic field follows from $F(A)$ and A:

$$\mathbf{B} = \frac{1}{r \sin \theta} \left[\frac{1}{r} \frac{\partial A}{\partial \theta} \hat{\mathbf{r}} - \frac{\partial A}{\partial r} \hat{\boldsymbol{\theta}} + F(A) \hat{\boldsymbol{\phi}} \right]. \quad (\text{A2})$$

For an untwisted magnetosphere, $F(A) = 0$. With the separable solutions of the form

$$A = r^{-n} f(\cos \theta), \quad (\text{A3})$$

there is an ordinary differential equation (Low & Lou 1990)

$$(1-x^2)f''(x) + n(n+1)f(x) = 0, \quad (\text{A4})$$

where n is a constant denoting the field configuration, i.e., $n=1$ for dipole, $n=2$ for quadrupole, etc. Therefore, the magnetic field can be described as

$$\mathbf{B} = \frac{1}{r^{2+n}} \left[-\frac{\partial f}{\partial \cos \theta} \hat{\mathbf{r}} + n \frac{f}{\sin \theta} \hat{\boldsymbol{\theta}} \right]. \quad (\text{A5})$$

The magnetic field lines satisfy

$$\frac{dr}{rd\theta} = \frac{\partial f}{nf\partial\theta}. \quad (\text{A6})$$

One can define R_{\max} , which denotes the largest distance from the stellar center at which the field line crosses the plane with colatitude of θ_{\max} . For certain field lines with R_{\max} , we can obtain

$$\frac{r}{R_{\max}} = \left[\frac{f(\theta)}{f(\theta_{\max})} \right]^{1/n}, \quad (\text{A7})$$

and

$$\tan \Theta = \frac{f' \sin \theta + nf \cos \theta}{f' \cos \theta - nf \sin \theta}. \quad (\text{A8})$$

where Θ is the angle between the magnetic axis and the tangent direction of magnetic field lines and f' denotes the derivative of f with respect to θ . From Equation (A8), the tangential direction for a certain field line only depends on θ rather than r . Basically, the curvature radius at (r, θ) is given by

$$\rho = \frac{(r^2 + r'^2)^{3/2}}{|r^2 + 2r'^2 - rr''|} = C_n(\theta)r, \quad (\text{A9})$$

where

$$C_n(\theta) = \frac{[1 + (f'/nf)^2]^{3/2}}{|1 + (f'/nf)^2 - f''/nf + f'^2/nf^2|}. \quad (\text{A10})$$

The distance that charges travel from θ_0 to θ is given by

$$s = \int_{\theta_0}^{\theta} \sqrt{dr^2 + r^2 d\theta^2} = r I_n(\theta, \theta_0), \quad (\text{A11})$$

where

$$I_n(\theta, \theta_0) = \left[\frac{1}{f(\theta)} \right]^{1/n} \times \int_{\theta_0}^{\theta} [f(\theta')]^{1/n} \sqrt{1 + \frac{1}{n^2 f(\theta')^2} \left(\frac{\partial f}{\partial \theta'} \right)^2} d\theta', \quad (\text{A12})$$

is a dimensionless parameter denoting the enhancement factor due to field line curvature. We define $I(\theta) = I_n(\theta, 0)$. The angle between radial direction and tangent direction of magnetic field lines is given by

$$\cos \theta_p = \frac{f'}{\sqrt{f'^2 + n^2 f^2}}. \quad (\text{A13})$$

In general, a bunch, as shown in Figure 1, can be simply adopted as a cuboid. Their length, height, and width are approximately $\lambda/2$, $r\Delta\theta$, and $2\varphi_r r$, leading to the cuboid volume of $V_b \simeq \varphi_r r^2 \lambda \Delta\theta \simeq \varphi_r r^2 \lambda [f'(\theta_s)/f''(\theta)] \Delta\theta_s$.

Appendix B Coherent Radiation from Moving Charges

In this section, we briefly summarize the physics of radiation from moving charges. Define $\beta_{e\perp}$ as the component of β_e in the plane that is perpendicular to the LOS:

$$\beta_{e\perp} = -\mathbf{n} \times (\mathbf{n} \times \beta_e). \quad (\text{B1})$$

For a single charge, the energy radiated per unit solid angle per unit frequency interval is given by (e.g., Rybicki & Lightman 1979; Jackson 1998)

$$\begin{aligned} \frac{d^2 W}{d\omega d\Omega} &= \frac{e^2 \omega^2}{4\pi^2 c} \left| \int_{-\infty}^{+\infty} -\beta_{e\perp} e^{i\omega(t-nr(t)/c)} dt \right|^2 \\ &= \frac{e^2 \omega^2}{4\pi^2 c} |\epsilon_{\parallel} A_{\parallel} + \epsilon_{\perp} A_{\perp}|^2, \end{aligned} \quad (\text{B2})$$

where ϵ_{\parallel} is the unit vector pointing to the center of the instantaneous circle, $\epsilon_{\perp} = \mathbf{n} \times \epsilon_{\parallel}$ is defined, and A_{\parallel} and A_{\perp} are the polarized components of the amplitude along ϵ_{\parallel} and ϵ_{\perp} , respectively.

As shown in Figure 12, for one trajectory, the angle between the electron velocity direction and x -axis at $t=0$ is defined as χ_{ij} , and that between the LOS and the trajectory plane is φ_k . Therefore, we have

$$\begin{aligned} \mathbf{n} \times (\mathbf{n} \times \beta_{e,ijk}) &= \beta_e \left[-\epsilon_{\parallel} \sin \left(\frac{v_e t}{\rho} + \chi_{ij} \right) \right. \\ &\quad \left. + \epsilon_{\perp} \cos \left(\frac{v_e t}{\rho} + \chi_{ij} \right) \sin \varphi_k \right], \end{aligned} \quad (\text{B3})$$

and

$$\begin{aligned} \omega \left(t - \frac{\mathbf{n} \cdot \mathbf{r}_{ijk}(t)}{c} \right) &= \omega \left[t - \frac{2\rho}{c} \sin \left(\frac{v_e t}{2\rho} \right) \cos \left(\frac{v_e t}{2\rho} + \chi_{ij} \right) \cos \varphi_k \right] \\ &\simeq \frac{\omega}{2} \left[\left(\frac{1}{\gamma^2} + \varphi_k^2 + \chi_{ij}^2 \right) t + \frac{c^2 t^3}{3\rho^2} + \frac{ct^2}{\rho} \chi_{ij} \right]. \end{aligned} \quad (\text{B4})$$

The amplitudes for one positron are given by

$$\begin{aligned} A_{\parallel,ijk} &\simeq \int_{-\infty}^{\infty} \left(\frac{ct}{\rho} + \chi_{ij} \right) \\ &\quad \times \exp \left(i \frac{\omega}{2} \left[\left(\frac{1}{\gamma^2} + \varphi_k^2 + \chi_{ij}^2 \right) t \right. \right. \\ &\quad \left. \left. + \frac{c^2 t^3}{3\rho^2} + \frac{ct^2}{\rho} \chi_{ij} \right] \right) dt, \\ A_{\perp,ijk} &\simeq \varphi_k \int_{-\infty}^{\infty} \\ &\quad \times \exp \left(i \frac{\omega}{2} \left[\left(\frac{1}{\gamma^2} + \varphi_k^2 + \chi_{ij}^2 \right) t \right. \right. \\ &\quad \left. \left. + \frac{c^2 t^3}{3\rho^2} + \frac{ct^2}{\rho} \chi_{ij} \right] \right) dt. \end{aligned} \quad (\text{B5})$$

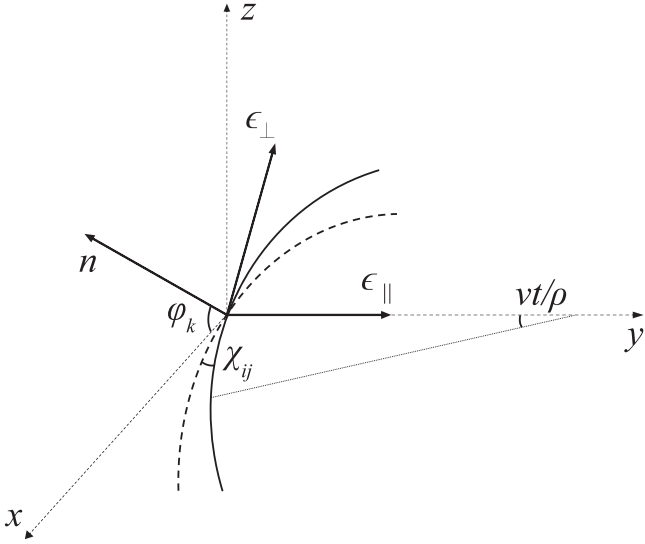


Figure 12. Geometry for instantaneous circular motion. The trajectory lies in the x - y plane. At the retarded time $t = 0$, the positron is at the origin. The dashed trajectory shows a positron at the origin, and the velocity is along the x -axis. The angle between the solid and dashed trajectory is χ_{ij} at $t = 0$. The angle between LOS and the trajectory plane is φ_k .

The introduction of the parameter u and ξ , i.e.,

$$u = \frac{ct}{\rho} \left(\frac{1}{\gamma^2} + \varphi_k^2 + \chi_{ij}^2 \right)^{-1/2},$$

$$\xi = \frac{\omega\rho}{3c} \left(\frac{1}{\gamma^2} + \varphi_k^2 + \chi_{ij}^2 \right)^{3/2}, \quad (\text{B6})$$

allows us to transform the polarized components of the amplitude into the form:

$$A_{\parallel,ijk} \simeq \frac{\rho}{c} \left(\frac{1}{\gamma^2} + \varphi_k^2 + \chi_{ij}^2 \right) \times \int_{-\infty}^{\infty} \left(u + \frac{\chi_{ij}}{\sqrt{1/\gamma^2 + \varphi_k^2 + \chi_{ij}^2}} \right) \times \exp \left(i \frac{3}{2} \xi \left(u + \frac{1}{3} u^3 + \frac{\chi_{ij}}{\sqrt{1/\gamma^2 + \varphi_k^2 + \chi_{ij}^2}} u^2 \right) \right) du,$$

$$A_{\perp,ijk} \simeq \frac{\rho}{c} \varphi_k \left(\frac{1}{\gamma^2} + \varphi_k^2 + \chi_{ij}^2 \right)^{1/2} \int_{-\infty}^{\infty} \exp \left(i \frac{3}{2} \xi \left(u + \frac{1}{3} u^3 + \frac{\chi_{ij}}{\sqrt{1/\gamma^2 + \varphi_k^2 + \chi_{ij}^2}} u^2 \right) \right) du. \quad (\text{B7})$$

Note that

$$\lim_{u \rightarrow +0} \left(u + \frac{1}{3} u^3 + \frac{\chi_{ij}}{\sqrt{1/\gamma^2 + \varphi_k^2 + \chi_{ij}^2}} u^2 \right) = u,$$

$$\lim_{u \rightarrow +\infty} \left(u + \frac{1}{3} u^3 + \frac{\chi_{ij}}{\sqrt{1/\gamma^2 + \varphi_k^2 + \chi_{ij}^2}} u^2 \right) = \frac{1}{3} u^3. \quad (\text{B8})$$

Therefore, the amplitudes in the above equation are given by

$$A_{\parallel,ijk} \simeq \frac{i2}{\sqrt{3}} \frac{\rho}{c} \left(\frac{1}{\gamma^2} + \varphi_k^2 + \chi_{ij}^2 \right) K_{\frac{2}{3}}(\xi) + \frac{2}{\sqrt{3}} \frac{\rho}{c} \chi_{ij} \left(\frac{1}{\gamma^2} + \varphi_k^2 + \chi_{ij}^2 \right)^{1/2} K_{\frac{1}{3}}(\xi),$$

$$A_{\perp,ijk} \simeq \frac{2}{\sqrt{3}} \frac{\rho}{c} \varphi_k \left(\frac{1}{\gamma^2} + \varphi_k^2 + \chi_{ij}^2 \right)^{1/2} K_{\frac{1}{3}}(\xi), \quad (\text{B9})$$

where $K_\nu(\xi)$ is the modified Bessel function.

For a single charge with identifiers i, j, k , the energy radiated per unit solid angle per unit frequency interval can be written as

$$\frac{d^2W}{d\omega d\Omega} \simeq \frac{e^2}{3\pi^2 c} \left(\frac{\omega\rho}{c} \right)^2 \left(\frac{1}{\gamma^2} + \varphi_k^2 + \chi_{ij}^2 \right)^2 \times \left[K_{\frac{2}{3}}^2(\xi) + \frac{\varphi_k^2 + \chi_{ij}^2}{1/\gamma^2 + \varphi_k^2 + \chi_{ij}^2} K_{\frac{1}{3}}^2(\xi) \right]. \quad (\text{B10})$$

The circular polarization fraction is given by

$$\frac{V}{I} = \frac{2\varphi_k (1/\gamma^2 + \varphi_k^2 + \chi_{ij}^2)^{1/2} K_{\frac{2}{3}}(\xi) K_{\frac{1}{3}}(\xi)}{K_{\frac{2}{3}}^2(\xi)/\gamma^2 + (\varphi_k^2 + \chi_{ij}^2) [K_{\frac{2}{3}}^2(\xi) + K_{\frac{1}{3}}^2(\xi)]}. \quad (\text{B11})$$

The 100% linear polarization appears at $\varphi_k = 0$ and circular polarization becomes stronger as φ_k gets larger.

We assume that the curvature radius is a constant in the bulk and each bunch has roughly the same $\chi_{u,i}$ and $\chi_{d,i}$. Then, one can derive average heights to replace the complex boundary condition of the bulk, shown in Figure 1. For more than one charged particle, a coherent summation of the amplitudes should replace the single amplitude. The total amplitude of i th bunch projection at the plane perpendicular to the LOS is then given by

$$A_{\parallel,i} \simeq \frac{2}{\sqrt{3}} \frac{\rho}{c} \frac{N_\theta}{\Delta\theta_s} \frac{N_\phi}{2\varphi_t} \int_{\chi_{d,i}}^{\chi_{u,i}} d\chi' \times \int_{\varphi_d}^{\varphi_u} \left[i \left(\frac{1}{\gamma^2} + \varphi'^2 + \chi'^2 \right) K_{\frac{2}{3}}(\xi) + \chi' \left(\frac{1}{\gamma^2} + \varphi'^2 + \chi'^2 \right)^{1/2} K_{\frac{1}{3}}(\xi) \right] \cos \varphi' d\varphi',$$

$$A_{\perp,i} \simeq \frac{2}{\sqrt{3}} \frac{\rho}{c} \frac{N_\theta}{\Delta\theta_s} \frac{N_\phi}{2\varphi_t} \int_{\chi_{d,i}}^{\chi_{u,i}} d\chi' \times \int_{\varphi_d}^{\varphi_u} \left(\frac{1}{\gamma^2} + \varphi'^2 + \chi'^2 \right)^{1/2} \times K_{\frac{1}{3}}(\xi) \varphi' \cos \varphi' d\varphi'. \quad (\text{B12})$$

For any $\varphi' \ll 1/\gamma$ and $\chi' \ll 1/\gamma$, the radiation emits within a conal angle $1/\gamma$. If $\omega \gg \omega_c$, one has $\xi \approx \omega/(2\omega_c) \gg 1$, leading to $K_\nu(\xi) \rightarrow \sqrt{\pi/2\xi} \exp(-\xi)$.

Therefore, one has approximately

$$\begin{aligned}
A_{\parallel,i} &\simeq (\varphi_u - \varphi_d) \frac{N_\theta}{\Delta\theta_s} \frac{N_\phi}{2\varphi_t} \frac{2}{\sqrt{3}} \frac{\rho}{\gamma c} \sqrt{\frac{\pi\omega_c}{\omega}} \\
&\times \exp\left(-\frac{\omega}{2\omega_c}\right) \left[i \frac{\chi_{u,i} - \chi_{d,i}}{\gamma} + \frac{\chi_{u,i}^2 - \chi_{d,i}^2}{2} \right], \\
A_{\perp,i} &\simeq \frac{N_\theta}{\Delta\theta_s} \frac{N_\phi}{2\varphi_t} \frac{2}{\sqrt{3}} \frac{\rho}{\gamma c} \sqrt{\frac{\pi\omega_c}{\omega}} \\
&\times \exp\left(-\frac{\omega}{2\omega_c}\right) (\chi_{u,i} - \chi_{d,i}) \left[\frac{\varphi_u^2 - \varphi_d^2}{2} \right].
\end{aligned} \tag{B13}$$

If $\omega \ll \omega_c$, the amplitudes read

$$\begin{aligned}
A_{\parallel,i} &\simeq (\varphi_u - \varphi_d) \frac{N_\theta}{\Delta\theta_s} \frac{N_\phi}{2\varphi_t} \frac{1}{\sqrt{3}} \frac{\rho}{\gamma c} \\
&\times \left[i \frac{\chi_{u,i} - \chi_{d,i}}{\gamma} \Gamma(2/3) \left(\frac{\omega}{4\omega_c}\right)^{-2/3} \right. \\
&\quad \left. + \frac{\chi_{u,i}^2 - \chi_{d,i}^2}{2} \Gamma(1/3) \left(\frac{\omega}{4\omega_c}\right)^{-1/3} \right], \\
A_{\perp,i} &\simeq \frac{N_\theta}{\Delta\theta_s} \frac{N_\phi}{2\varphi_t} \frac{1}{\sqrt{3}} \frac{\rho}{\gamma c} (\chi_{u,i} - \chi_{d,i}) \\
&\times \Gamma(1/3) \left(\frac{\omega}{4\omega_c}\right)^{-1/3} \left[\frac{\varphi_u^2 - \varphi_d^2}{2} \right],
\end{aligned} \tag{B14}$$

where $\Gamma(\nu)$ is the Gamma function. In the scenario that $\varphi' \ll 1/\gamma$ and $\chi' \ll 1/\gamma$, only the imaginary component in Equation (B14) plays an important role on amplitude. As shown in Figure 1, the limitations of φ' read $\varphi_u = \varphi_t + \varphi$ and $\varphi_d = -\varphi_t + \varphi$. Consequently, the total energy radiated per unit solid angle per unit frequency interval for charges in i th bunch is given by

$$\begin{aligned}
\left. \frac{d^2W}{d\omega d\Omega} \right|_i &\simeq \left(\frac{N_\theta N_\phi}{\Delta\theta_s} \right)^2 (\chi_{u,i} - \chi_{d,i})^2 \frac{3e^2\gamma^2}{4\pi^2 c} \\
&\times \begin{cases} 2^{2/3} \Gamma(2/3)^2 \left(\frac{\omega}{\omega_c}\right)^{2/3}, & \omega \ll \omega_c, \\ \pi \left(\frac{\omega}{\omega_c}\right) \exp\left(-\frac{\omega}{\omega_c}\right), & \omega \gg \omega_c. \end{cases}
\end{aligned} \tag{B15}$$

For any $\chi' \gg 1/\gamma \gg \varphi'$, the total amplitudes of the i th bunch projection on the plane perpendicular to a certain LOS can be written as

$$\begin{aligned}
A_{\parallel,i} &\simeq \frac{2}{\sqrt{3}} \frac{\rho}{c} \frac{N_\theta}{\Delta\theta_s} \frac{N_\phi}{2\varphi_t} \int_{\chi_{d,i}}^{\chi_{u,i}} d\chi' \int_{\varphi_d}^{\varphi_u} \\
&\times [i\chi'^2 K_{\frac{2}{3}}(\xi) + \chi'|K_{\frac{1}{3}}(\xi)] \cos \varphi' d\varphi', \\
A_{\perp,i} &\simeq \frac{2}{\sqrt{3}} \frac{\rho}{c} \frac{N_\theta}{\Delta\theta_s} \frac{N_\phi}{2\varphi_t} \int_{\chi_{d,i}}^{\chi_{u,i}} d\chi' \\
&\times \int_{\varphi_d}^{\varphi_u} |\chi'| K_{\frac{1}{3}}(\xi) \varphi' \cos \varphi' d\varphi'.
\end{aligned} \tag{B16}$$

If $\omega \ll \omega_t \ll \omega_c$, one has $\xi \approx \omega\rho|\chi'|^3/3c \ll 1$. The amplitudes are the same as Equation (B14). If $\omega_t \ll \omega \ll \omega_c$, the parallel amplitude is given by

$$\begin{aligned}
A_{\parallel,i} &\simeq (\varphi_u - \varphi_d) \frac{2}{\sqrt{3}} \frac{\rho}{c} \frac{N_\theta}{\Delta\theta_s} \frac{N_\phi}{2\varphi_t} \\
&\times \int_{\chi_{d,i}}^{\chi_{u,i}} (i\chi'^2 + \chi'|K_{\frac{1}{3}}(\xi)) \sqrt{\frac{3c\pi}{\omega\rho|\chi'|^3}} \\
&\times \exp\left(-\frac{\omega\rho|\chi'|^3}{3c}\right) d\chi'.
\end{aligned} \tag{B17}$$

Note that the error function is defined as

$$\text{erf}(x) = \frac{2}{\sqrt{\pi}} \int_0^x \exp(-\eta^2) d\eta. \tag{B18}$$

According to Equation (B17) and the properties of the error function, e.g., $\text{erf}(x) \rightarrow 1$ for $x \rightarrow +\infty$, one has

$$\begin{aligned}
A_{\parallel,i} &\simeq (\varphi_u - \varphi_d) \frac{i2\pi}{\sqrt{3}} \frac{1}{\omega} \frac{N_\theta}{\Delta\theta_s} \frac{N_\phi}{2\varphi_t} \\
&\times [\text{erf}(x_u) + \text{erf}(x_d)],
\end{aligned} \tag{B19}$$

where $x_u = (\rho\omega|\chi_u|^3/3c)^{1/2}$ and $x_d = (\rho\omega|\chi_d|^3/3c)^{1/2}$. $A_{\perp,i} \simeq 0$ due to $\varphi \ll \chi'$. The total energy radiated per unit solid angle per unit frequency interval for charges in i th bunch is given by

For $\varphi' \gg 1/\gamma \gg \chi'$, we can just exchange $\chi_{u,i}$ and $\chi_{d,i}$ with φ_u and φ_d in Equation (B20). Therefore, the total energy radiated per unit solid angle per unit frequency interval for

$$\begin{aligned}
\left. \frac{d^2W}{d\omega d\Omega} \right|_i &\simeq \left(\frac{N_\theta N_\phi}{\Delta\theta_s} \right)^2 (\chi_{u,i} - \chi_{d,i})^2 \frac{3e^2\gamma^2}{4\pi^2 c} \\
&\times \begin{cases} \Gamma(2/3)^2 \left(\frac{2\omega}{\omega_c}\right)^{2/3} + \frac{\gamma^2}{2^{2/3}} \left(\frac{\chi_{u,i} + \chi_{d,i}}{2}\right)^2 \Gamma(1/3)^2 \left(\frac{\omega}{\omega_c}\right)^{4/3}, & \omega \ll \omega_t, \\ \left[\frac{4\pi}{3\gamma(\chi_{u,i} - \chi_{d,i})} \right]^2, & \omega_t \ll \omega. \end{cases}
\end{aligned} \tag{B20}$$

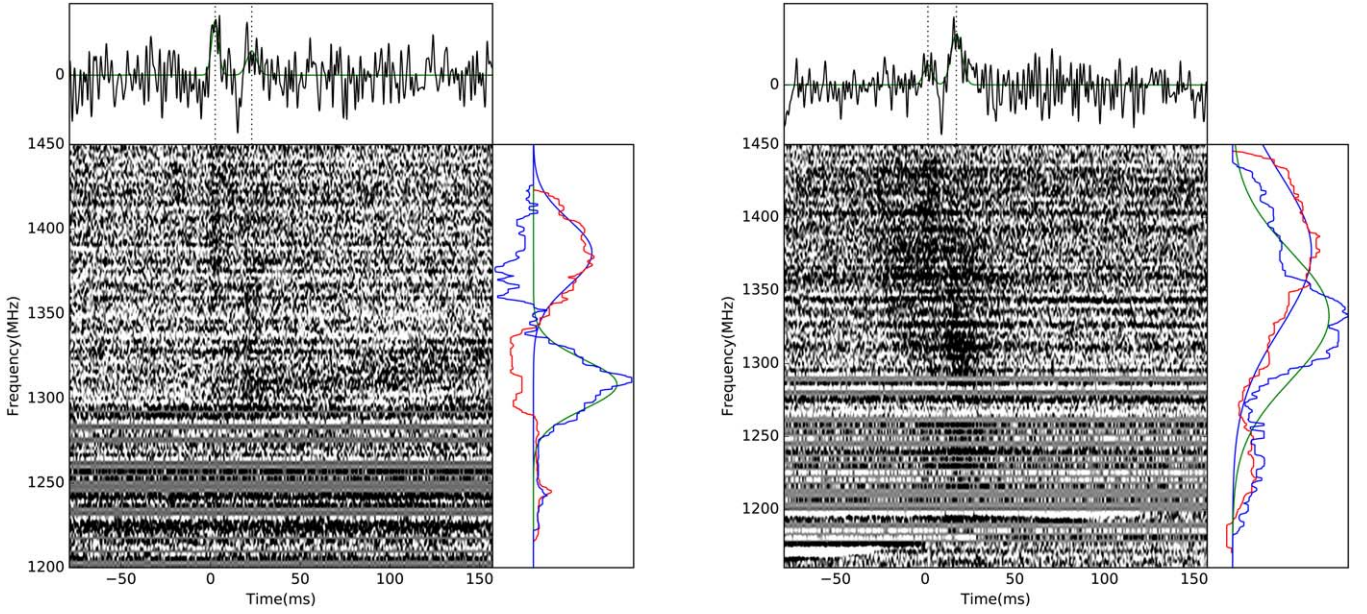


Figure 13. Dynamic spectra of two bursts from FRB 190520B. The upper subplot shows the pulse intensity varying with time, including the two subpulses and their Gaussian fit profiles. The middle plot shows the dynamic spectrum after dedispersion. The right plot shows the spectrum of each subpulse.

charges in the i th bunch is given by

$$\frac{d^2W}{d\omega d\Omega} \Big|_i \simeq \left(\frac{N_\theta N_\phi}{\Delta\theta_s} \right)^2 (\chi_{u,i} - \chi_{d,i})^2 \frac{3e^2\gamma^2}{4\pi^2 c} \times \begin{cases} \Gamma(2/3)^2 \left(\frac{2\omega}{\omega_c} \right)^{2/3} + \frac{\gamma^2}{2^{2/3}} \varphi^2 \Gamma(1/3)^2 \left(\frac{\omega}{\omega_c} \right)^{4/3}, & \omega \ll \omega_t, \\ \left(\frac{2\pi}{3\gamma\varphi_t} \right)^2, & \omega_t \ll \omega. \end{cases} \quad (\text{B21})$$

Only if the size of the charged particle bunch is much smaller than the half-wavelength can the phase of radiation from the particles be approximately the same, which allows the emission to be highly coherent. However, if $\omega \gg \omega_t$, the coherence of radiation would be reduced. According to Equation (20), the total energy radiated per unit solid angle per unit frequency interval for the moving bulk of bunches is given by

$$\frac{d^2W}{d\omega d\Omega} = \frac{e^2\omega^2}{4\pi^2 c} \left| \sum_i^{N_t} -\epsilon_{|A|,i} + \epsilon_{\perp A_{\perp},i} \right|^2 \simeq F_\omega(N_t, N_{lb}) \frac{e^2\omega^2}{4\pi^2 c} |-\epsilon_{|A|,i} + \epsilon_{\perp A_{\perp},i}|^2, \quad (\text{B22})$$

where $F_\omega(N_t, N_{lb})$ reads a dimensionless parameter denoting the enhancement factor due to coherence (Yang & Zhang 2018):

$$F_\omega(N_t, N_{lb}) = N_t^2 N_{lb}^2 \left[\frac{\sin(\pi l/\lambda)}{(\pi l/\lambda)} \right]^2 \times \left[\frac{\sin(\pi l_s/\lambda)}{(\pi l_s/\lambda)} \right]^2. \quad (\text{B23})$$

At higher frequencies, since oscillations become more rapid, the function could be approximated as a power law. If $l_s \ll \lambda$, the total intensity is proportional to $N_t^2 N_{lb}^2$. If $l \ll \lambda \ll l_s$, the

radiation from the bunches adds incoherently, i.e., $\mathcal{L} \propto N_{lb} N_t^2$. Once $\lambda \ll l$ is satisfied, the radiation would become totally incoherent.

Appendix C Data Analysis of FRB 190520B

In this section, we summarize the observation of an active repeating FRB source, namely FRB 190520B, newly discovered by FAST (Niu et al. 2021). The complex pulse morphology provides a way to reveal its intrinsic emission mechanism. 79 bursts have been analyzed and 13 of them are found to have accompanied pulse(s) detected within 200 ms. Among the 13 bursts, 11 of them still emit at the ends of the FAST frequency bandpass, so one is unable to measure their intrinsic frequency drift. We only keep the other two bursts for further calculations.

The dynamic spectral data has been dedispersed first according to their best DM. To find the center frequency and the arrival time of each sub-burst, we made a Gaussian fit both on their spectrum and pulse profile. We take the peak value of the Gaussian fit profile as the central frequency and arrival time. The pulse width and central frequency for the two sets of subpulses are [7.9, 11.4] ms [1386, 1308] MHz and [9.8, 12.1] ms [1376.8, 1332.7] MHz, respectively. Then, we got the frequency drift rates $-3.81 \text{ MHz ms}^{-1}$ and $-2.79 \text{ MHz ms}^{-1}$ for two sets of bursts from FRB 190520B. Figure 13 shows the frequency drift on the dynamic spectrum.

Appendix D Notation List

(Continued)

Symbol	Definition	First Appear	Symbol	Definition	First Appear
Subscript i, j, k	The identifier of each charged particle	Section 2.3, Appendix B	N_θ	Maximum number of the subscript of j	Section 2.3, Appendix B
Subscript x	x is a number denoting the order of magnitude	Section 1	P	Period of a neutron star	Section 2.1
a	Strength parameter	Section 2.2	P_{gas}	Gas pressure	Equation (16)
c	Speed of light	Section 2.1, Appendix B	P_{rad}	Radiation pressure	Equation (15)
$d^2W/d\omega d\Omega$	Energy radiated per unit solid angle per unit frequency interval	Equation (18), Appendix B	R	Stellar radius	Section 2.1
e	Elementary charge	Section 2.1, Appendix B	\mathcal{R}	Distance from the emitting source to the observer	Section 2.3
l	Length of a bunch	Section 2.1, Appendix B	T	Mean time interval between adjacent bunches	Section 2.3
l_s	Mean space between neighborhood bunches	Section 2.1, Appendix B	V_b	Volume of a bunch	Equation (2)
m_e	Electron/positron mass	Section 2.1	α	Angle between the magnetic axis and the rotational axis	Section 2
\mathbf{n}	Unit vector of the line of sight	Appendix B	β_e	Dimensionless velocity of a positron	Section 2.3, Appendix A
n	A constant denoting the field configuration	Section 2.1, Appendix A	γ	Lorentz factor	Section 2, Appendix B
n_e	Number density of net charge	Equation (9)	λ	Wavelength	Section 2.3, Appendix B
n_{GJ}	Goldreich–Julian density	Equation (11)	μ	A proportionality factor	Equation (29)
r	Distance to the neutron star center	Section 2	ν	Frequency	Section 2
s	Distance that charges traveled along the field lines	Section 2.1, Equation (A11)	$\dot{\nu}$	Drift rate	Section 3.1
t_c	Cooling timescale	Equation (7)	χ	Angle between the electron velocity direction for different trajectories	Section 2, Appendix B
t_{int}	Burst intrinsic duration	Section 2.1	χ_d	Lower boundary of χ	Section 2.3, Appendix B
v_e	Velocity of positron	Section 2.1, Appendix B	χ_u	Upper boundary of χ	Section 2.3, Appendix B
w	Subpulse width	Section 2.1	ψ	Polarization angle due to the rotation vector model	Equation (32)
z	Redshift	Section 2.1	ρ	Curvature radius	Section 2, Appendix B
A	Flux function	Appendix A	σ	Scattering cross section	Section 2.2
A_{\parallel}	Parallel component of amplitude	Section 2.3, Appendix B	σ_T	Thomson cross section	Section 2.2
A_{\perp}	Perpendicular component of amplitude	Section 2.3, Appendix B	σ_w	Gaussian width	Equation (33)
B	Magnetic field strength	Section 2	θ	Poloidal angle with respect to the magnetic axis	Section 2, Appendix A
B_s	Magnetic field strength at stellar surface	Section 2.1	θ_e	Spread angle of the curvature radiation	Equation (21)
$C_n(\theta)$	A geometric factor	Equation (A10)	θ_{jet}	Burst “jet” beaming angle	Equation (1)
I, Q, U, V	Stokes parameters	Section 2.4, Appendix B	θ_p	Angle between radial direction and tangent direction of magnetic field lines	Section 3.1, Equation (A13)
E	Wave electric field	Section 2.1	θ_s	Angle of the footpoint for field line at the stellar surface	Section 2.1
E_{\parallel}	Electric field parallel to the B field	Section 2.1	ω	Angular frequency	Section 2.3, Appendix B
$F(A)$	Free function	Section A	ω_B	Cyclotron frequency	Equation (12)
K_ν	Modified Bessel function	Section 2.3, Appendix B	ω_c	Critical angle frequency of curvature radiation	Section 2.3, Appendix B
L	Linear polarization	Section 2.4	ω_l	Critical angle frequency for the bunch length	Equation (23), Appendix B
\mathcal{L}	Luminosity	Section 2.1	ω_t	Critical angle frequency for the trajectories	Section 2.3, Appendix B
\mathcal{L}_b	Luminosity of a bunch	Section 2.1	φ	Azimuth angle with respect to the magnetic axis	Section 2
\mathcal{L}_{iso}	Isotropic equivalent luminosity in the observer frame	Equation (4)	φ_t	Angle between LOS and the trajectory plane	Appendix B
p_e	Curvature radiation luminosity of a positron	Section 2.1	φ_t	Half opening angle of the bunches	Section 2.1, Appendix B
\mathcal{M}	Multiplicity	Equation (10)	ζ	Angle between the LOS and spin axis	Section 2.4
N_b	Number of bunches contributing to instantaneous radiation	Section 2.1	$\Gamma(\nu)$	Gamma function	Appendix B
N_B	Total number of bunch	Section 2.1, Appendix B	Φ	Azimuth angle with respect to the spin axis	Section 2.4
N_e	Number of net charges in one bunch	Section 2.1, Appendix B	Φ_p	Peak location of the Gaussian function	Equation (33)
N_s	Maximum number of the subscript of i	Section 2.3, Appendix B	Ψ	Polarization angle	Equation (30),
N_ϕ	Maximum number of the subscript of k	Section 2.3, Appendix B	Θ		Equation (A8)

(Continued)

Symbol	Definition	First Appear
Ω	The angle between magnetic axis and tangent direction of magnetic field lines	
	Angle frequency of a neutron star	Equation (11)
	Solid angle of radiation	Section 2, Appendix B

ORCID iDs

Renxin Xu (徐仁新)  <https://orcid.org/0000-0002-9042-3044>

References

- Asseo, E., & Melikidze, G. I. 1998, *MNRAS*, 301, 59
- Beloborodov, A. M. 2020, *ApJ*, 896, 142
- Beloborodov, A. M. 2021, *ApJL*, 922, L7
- Benáček, J., Muñoz, P. A., & Büchner, J. 2021, *ApJ*, 923, 99
- Bilous, A. V., Griessmeier, J. M., & Pennucci, T. 2022, *A&A*, 658, A143
- Bochenek, C. D., Ravi, V., Belov, K. V., et al. 2020, *Natur*, 587, 59
- Caleb, M., Stappers, B. W., Abbott, T. D., et al. 2020, *MNRAS*, 496, 4565
- Chamma, M. A., Rajabi, F., Wyenberg, C. M., Mathews, A., & Houde, M. 2021, *MNRAS*, 507, 246
- Chatterjee, S., Law, C. J., Wharton, R. S., et al. 2017, *Natur*, 541, 58
- Chawla, P., Andersen, B. C., Bhardwaj, M., et al. 2020, *ApJL*, 896, L41
- Cheng, A. F., & Ruderman, M. A. 1977, *ApJ*, 212, 800
- CHIME/FRB Collaboration, Amiri, M., Bandura, K., et al. 2019a, *Natur*, 566, 235
- CHIME/FRB Collaboration, Andersen, B. C., Bandura, K., et al. 2019b, *ApJL*, 885, L24
- CHIME/Frb Collaboration, Amiri, M., Andersen, B. C., et al. 2020a, *Natur*, 582, 351
- CHIME/FRB Collaboration, Andersen, B. C., Bandura, K. M., et al. 2020b, *Natur*, 587, 54
- CHIME/FRB Collaboration, Amiri, M., Andersen, B. C., et al. 2021, *ApJS*, 257, 59
- Cho, H., Macquart, J.-P., Shannon, R. M., et al. 2020, *ApJL*, 891, L38
- Cooper, A. J., & Wijers, R. A. M. J. 2021a, *MNRAS*, 508, L32
- Cooper, A. J., & Wijers, R. A. M. J. 2021b, arXiv:2110.15244
- Cordes, J. M., & Chatterjee, S. 2019, *ARA&A*, 57, 417
- Cordes, J. M., Ocker, S. K., & Chatterjee, S. 2021, arXiv:2108.01172
- Cordes, J. M., Wasserman, I., Hessels, J. W. T., et al. 2017, *ApJ*, 842, 35
- Dai, S., Lu, J., Wang, C., et al. 2021, *ApJ*, 920, 46
- Day, C. K., Deller, A. T., Shannon, R. M., et al. 2020, *MNRAS*, 497, 3335
- Deng, W., & Zhang, B. 2014, *ApJL*, 783, L35
- Elsaesser, K., & Kirk, J. 1976, *A&A*, 52, 449
- Fonseca, E., Andersen, B. C., Bhardwaj, M., et al. 2020, *ApJL*, 891, L6
- Gajjar, V., Siemion, A. P. V., Price, D. C., et al. 2018, *ApJ*, 863, 2
- Gangadhara, R. T., Han, J. L., & Wang, P. F. 2021, *ApJ*, 911, 152
- Ghisellini, G., & Locatelli, N. 2018, *A&A*, 613, A61
- Gil, J., Lyubarsky, Y., & Melikidze, G. I. 2004, *ApJ*, 600, 872
- Goldreich, P., & Julian, W. H. 1969, *ApJ*, 157, 869
- Hilmarsson, G. H., Michilli, D., Spitler, L. G., et al. 2021a, *ApJL*, 908, L10
- Hilmarsson, G. H., Spitler, L. G., Main, R. A., & Li, D. Z. 2021b, *MNRAS*, 508, 5354
- Hessels, J. W. T., Spitler, L. G., Seymour, A. D., et al. 2019, *ApJL*, 876, L23
- Ioka, K. 2020, *ApJL*, 904, L15
- Jackson, J. D. 1998, *Classical Electrodynamics*, 3rd Edition, by John David Jackson (New York: Wiley-VCH) p 832
- Josephy, A., Chawla, P., Fonseca, E., et al. 2019, *ApJL*, 882, L18
- Katz, J. I. 2014, *PhRvD*, 89, 103009
- Katz, J. I. 2018, *MNRAS*, 481, 2946
- Kumar, P., Lu, W., & Bhattacharya, M. 2017, *MNRAS*, 468, 2726
- Kumar, P., & Bošnjak, Ž. 2020, *MNRAS*, 494, 2385
- Kumar, P., Shannon, R. M., Lower, M. E., et al. 2021, arXiv:2109.11535
- Kundu, E., & Zhang, B. 2021, *MNRAS*, 508, L48
- Li, D., Wang, P., Zhu, W. W., et al. 2021, *Natur*, 598, 267
- Liu, Z.-N., Wang, W.-Y., Yang, Y.-P., & Dai, Z.-G. 2020, *ApJ*, 905, 140
- Lorimer, D. R., & Kramer, M. 2012, in *Handbook of Pulsar Astronomy*, ed. D. R. Lorimer & M. Kramer (Cambridge: Cambridge Univ. Press)
- Lorimer, D. R., Bailes, M., McLaughlin, M. A., Narkevic, D. J., & Crawford, F. 2007, *Sci*, 318, 777
- Low, B. C., & Lou, Y. Q. 1990, *ApJ*, 352, 343
- Lu, W., & Kumar, P. 2018, *MNRAS*, 477, 2470
- Lu, W., Kumar, P., & Zhang, B. 2020, *MNRAS*, 498, 1397
- Luo, R., Wang, B. J., Men, Y. P., et al. 2020, *Natur*, 586, 693
- Margalit, B., Beniamini, P., Sridhar, N., & Metzger, B. D. 2020, *ApJL*, 899, L27
- Melikidze, G. I., Gil, J. A., & Pataraya, A. D. 2000, *ApJ*, 544, 1081
- Melrose, D. B. 2017, *RvMPP*, 1, 5
- Metzger, B. D., Margalit, B., & Sironi, L. 2019, *MNRAS*, 485, 4091
- Michilli, D., Seymour, A., Hessels, J. W. T., et al. 2018, *Natur*, 553, 182
- Nimmo, K., Hessels, J. W. T., Keimpema, A., et al. 2021, *NatAs*, 5, 594
- Niu, C.-H., Aggarwal, K., Li, D., et al. 2021, arXiv:2110.07418
- Pastor-Marazuela, I., Connor, L., van Leeuwen, J., et al. 2021, *Natur*, 596, 505
- Petroff, E., Hessels, J. W. T., & Lorimer, D. R. 2019, *A&ARv*, 27, 4
- Philippov, A., Timokhin, A., & Spitkovsky, A. 2020, *PhRvL*, 124, 245101
- Platts, E., Weltman, A., Walters, A., et al. 2019, *PhR*, 821, 1
- Platts, E., Caleb, M., Stappers, B. W., et al. 2021, *MNRAS*, 505, 3041
- Pleunis, Z., Good, D. C., Kaspi, V. M., et al. 2021, *ApJ*, 923, 1
- Pol, N., Lam, M. T., McLaughlin, M. A., Lazio, T. J. W., & Cordes, J. M. 2019, *ApJ*, 886, 135
- Radhakrishnan, V., & Cooke, D. J. 1969, *ApJL*, 3, 225
- Rajabi, F., Chamma, M. A., Wyenberg, C. M., Mathews, A., & Houde, M. 2020, *MNRAS*, 498, 4936
- Ruderman, M. A., & Sutherland, P. G. 1975, *ApJ*, 196, 51
- Rybicki, G. B., & Lightman, A. P. 1979, *A Wiley-Interscience Publication* (New York: Wiley)
- Simard, D., & Ravi, V. 2020, *ApJL*, 899, L21
- Spitler, L. G., Scholz, P., Hessels, J. W. T., et al. 2016, *Natur*, 531, 202
- Sturrock, P. A., Petrosian, V., & Turk, J. S. 1975, *ApJ*, 196, 73
- Usov, V. V. 1987, *ApJ*, 320, 333
- Wang, J.-S., & Lai, D. 2020, *ApJ*, 892, 135
- Wang, W., Zhang, B., Chen, X., & Xu, R. 2019, *ApJL*, 876, L15
- Wang, W.-Y., Xu, R., & Chen, X. 2020, *ApJ*, 899, 109
- Xu, H., Niu, J. R., Chen, P., et al. 2021, arXiv:2111.11764
- Yang, Y.-P., & Zhang, B. 2018, *ApJ*, 868, 31
- Yang, Y.-P., Zhang, B., & Wei, J.-Y. 2019, *ApJ*, 878, 89
- Yang, Y.-P., Zhu, J.-P., Zhang, B., & Wu, X.-F. 2020, *ApJL*, 901, L13
- Yang, Y.-P., & Zhang, B. 2020, *ApJL*, 892, L10
- Yang, Y.-P., & Zhang, B. 2021, *ApJ*, 919, 89
- Zhang, B. 2018, *ApJL*, 867, L21
- Zhang, B. 2020, *Natur*, 587, 45
- Zhang, B. 2022, *ApJ*, 925, 53